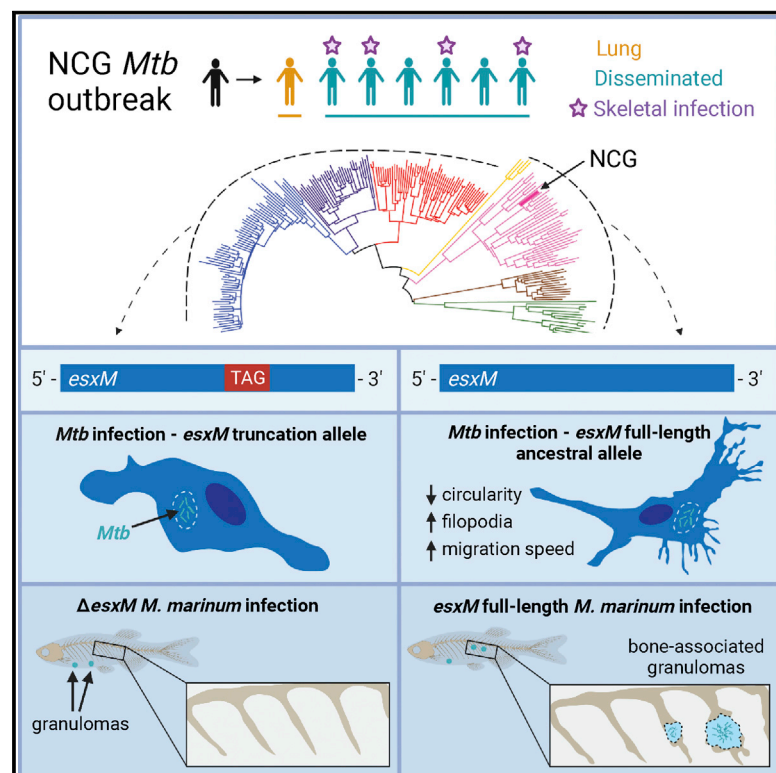


An ancestral mycobacterial effector promotes dissemination of infection

Graphical abstract



Authors

Joseph W. Saelens, Mollie I. Sweeney, Gopinath Viswanathan, ..., Sunhee Lee, Jason E. Stout, David M. Tobin

Correspondence

sunhlee@utmb.edu (S.L.), jason.stout@duke.edu (J.E.S.), david.tobin@duke.edu (D.M.T.)

In brief

Tuberculosis outbreak with a unique clinical manifestation unveils previously unappreciated insights into pathogen evolution and host-pathogen interactions.

Highlights

- High rates of disseminated and skeletal disease during a tuberculosis outbreak
- Lineage 1 strains of *Mycobacterium tuberculosis* carry the ancestral version of EsxM
- Ancestral, full-length EsxM alters the macrophage cytoskeleton and enhances motility
- Ancestral EsxM promotes granuloma efflux, dissemination, and bone disease

Article

An ancestral mycobacterial effector promotes dissemination of infection

Joseph W. Saelens,^{1,9} Mollie I. Sweeney,^{1,9} Gopinath Viswanathan,^{1,9} Ana María Xet-Mull,¹ Kristen L. Jurcic Smith,¹ Dana M. Sisk,¹ Daniel D. Hu,² Rachel M. Cronin,³ Erika J. Hughes,¹ W. Jared Brewer,¹ Jörn Coers,^{1,4} Matthew M. Champion,^{2,5} Patricia A. Champion,^{3,5} Craig B. Lowe,¹ Clare M. Smith,¹ Sunhee Lee,^{1,6,7,*} Jason E. Stout,^{6,8,*} and David M. Tobin^{1,4,10,*}

¹Department of Molecular Genetics and Microbiology, Duke University School of Medicine, Durham, NC 27710, USA

²Department of Chemistry and Biochemistry, University of Notre Dame, Notre Dame, IN 46556, USA

³Department of Biological Sciences, University of Notre Dame, Notre Dame, IN 46556, USA

⁴Department of Immunology, Duke University School of Medicine, Durham, NC 27710, USA

⁵Eck Institute for Global Health, University of Notre Dame, Notre Dame, IN 46556, USA

⁶Department of Medicine, Duke University School of Medicine, Durham, NC 27710, USA

⁷Department of Microbiology and Immunology, University of Texas Medical Branch, Galveston, TX 77555, USA

⁸Division of Infectious Diseases and International Health, Duke University School of Medicine, Durham, NC 27710, USA

⁹These authors contributed equally

¹⁰Lead contact

*Correspondence: sunhlee@utmb.edu (S.L.), jason.stout@duke.edu (J.E.S.), david.tobin@duke.edu (D.M.T.)

<https://doi.org/10.1016/j.cell.2022.10.019>

SUMMARY

The human pathogen *Mycobacterium tuberculosis* typically causes lung disease but can also disseminate to other tissues. We identified a *M. tuberculosis* (*Mtb*) outbreak presenting with unusually high rates of extrapulmonary dissemination and bone disease. We found that the causal strain carried an ancestral full-length version of the type VII-secreted effector EsxM rather than the truncated version present in other modern *Mtb* lineages. The ancestral EsxM variant exacerbated dissemination through enhancement of macrophage motility, increased egress of macrophages from established granulomas, and alterations in macrophage actin dynamics. Reconstitution of the ancestral version of EsxM in an attenuated modern strain of *Mtb* altered the migratory mode of infected macrophages, enhancing their motility. In a zebrafish model, full-length EsxM promoted bone disease. The presence of a derived nonsense variant in EsxM throughout the major *Mtb* lineages 2, 3, and 4 is consistent with a role for EsxM in regulating the extent of dissemination.

INTRODUCTION

Mycobacterium tuberculosis (*Mtb*), the etiologic agent of the disease tuberculosis (TB), is a pathogen of critical public health importance.¹ TB is predominantly a pulmonary disease, but 15%–20% of cases present with extrapulmonary manifestations.² Extrapulmonary infections can be difficult to diagnose and treat. Skeletal TB, in turn, is a relatively uncommon manifestation of extrapulmonary TB, affecting only 148 of 7,174 (~2%) reported TB cases in the US in 2020.² Although skeletal TB, or Pott's Disease, has long been recognized, with characteristic TB-induced spinal deformities described in humans from as far back as ancient Egypt,³ the specific bacterial factors that influence dissemination, tissue tropism, and bone disease are not well characterized.

Upon its establishment as a distinct species, *Mtb* evolved largely clonally.^{4–7} Although horizontal gene transfer likely contributed to its initial evolution as a human pathogen,⁸ *Mtb* thereafter seems to have undergone relatively few horizontal gene transfer events, with some structural variants arising

through genomic deletions.^{7,9,10} *Mtb* has classically been grouped into at least seven discrete lineages. So-called “modern” lineages, which include lineages 2, 3, and 4, (L2, L3, and L4) are broadly distributed throughout the world.⁹ Other lineages (L1, L5, L6, and L7) are more geographically constrained.¹¹ L1 strains, although geographically limited, still account for many overall cases and have been previously reported to induce distinct inflammatory phenotypes and differentially modulate innate immune signaling in the human host.^{12–15}

Pathogenic mycobacteria achieve dissemination through a remarkable ability to spread within their hosts. They hijack host macrophages as both a major replicative niche and for delivery to distal locations within and between tissues.¹⁶ Macrophage function and motility influence dissemination of mycobacterial disease through a number of mechanisms, including macrophage survival and cell death, and efflux from initial nidi to new sites.^{17–20} The dynamics of granuloma formation, dissolution, and resolution also influence the trajectory of infection and dissemination in zebrafish and macaque models.^{21–24}

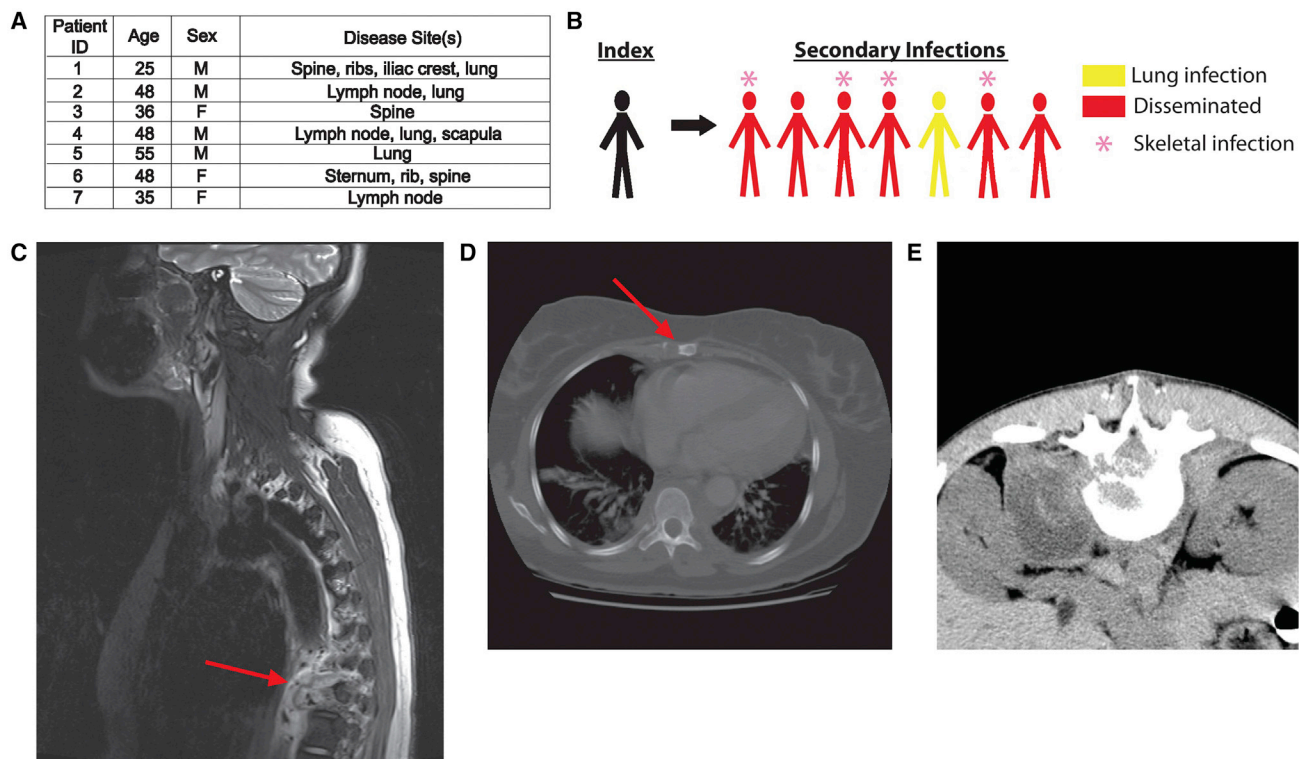


Figure 1. An outbreak in North Carolina with high rates of extrapulmonary and bone disease

(A) Characterization of all secondary cases of the NCG outbreak strain. All patients were HIV negative and had no known immunodeficiencies.

(B) Schematic depicting index and secondary cases in the NCG outbreak.

(C) Destructive lesion of T-spine vertebra 9 with extensive paraspinal abscess (red arrow) caused by *Mtb* NCG infection.

(D) Lytic lesion of the sternum (red arrow) caused by *Mtb* NCG infection.

(E) CT scan of paraspinal abscess caused by *Mtb* NCG infection.

Macrophage and granuloma behavior is heavily influenced by dedicated bacterial effectors secreted through type VII secretion systems. The ESX-1 system, notably absent in the attenuated BCG vaccine strain,^{25–28} plays multiple roles in virulence, most prominently in the permeabilization of the phagosomal membrane in infected macrophages.^{29–34} Mutants defective for the small secreted effectors specific to the ESX-1 secretion system—EsxA and EsxB—display altered virulence.³⁵ Similarly, the paralogous ESX-3 system regulates important pathogen–host interactions, including iron acquisition,^{36,37} and, through interactions of the small secreted effectors EsxG and EsxH with the ESCRT complex, host membrane trafficking, and damage response.^{38–40}

ESX-5, the most recently evolved of the paralogous type VII secretion systems, is found only in the slow-growing pathogenic mycobacteria, including *Mtb* and *Mycobacterium marinum*.^{41,42} ESX-5 has been implicated in secretion of *Mtb*'s abundant PE and PPE family proteins^{43,44} and the CpnT toxin.⁴⁵ However, a biological role of any of the small secreted effectors specific to ESX-5, including EsxM and EsxN, has not fully been examined.

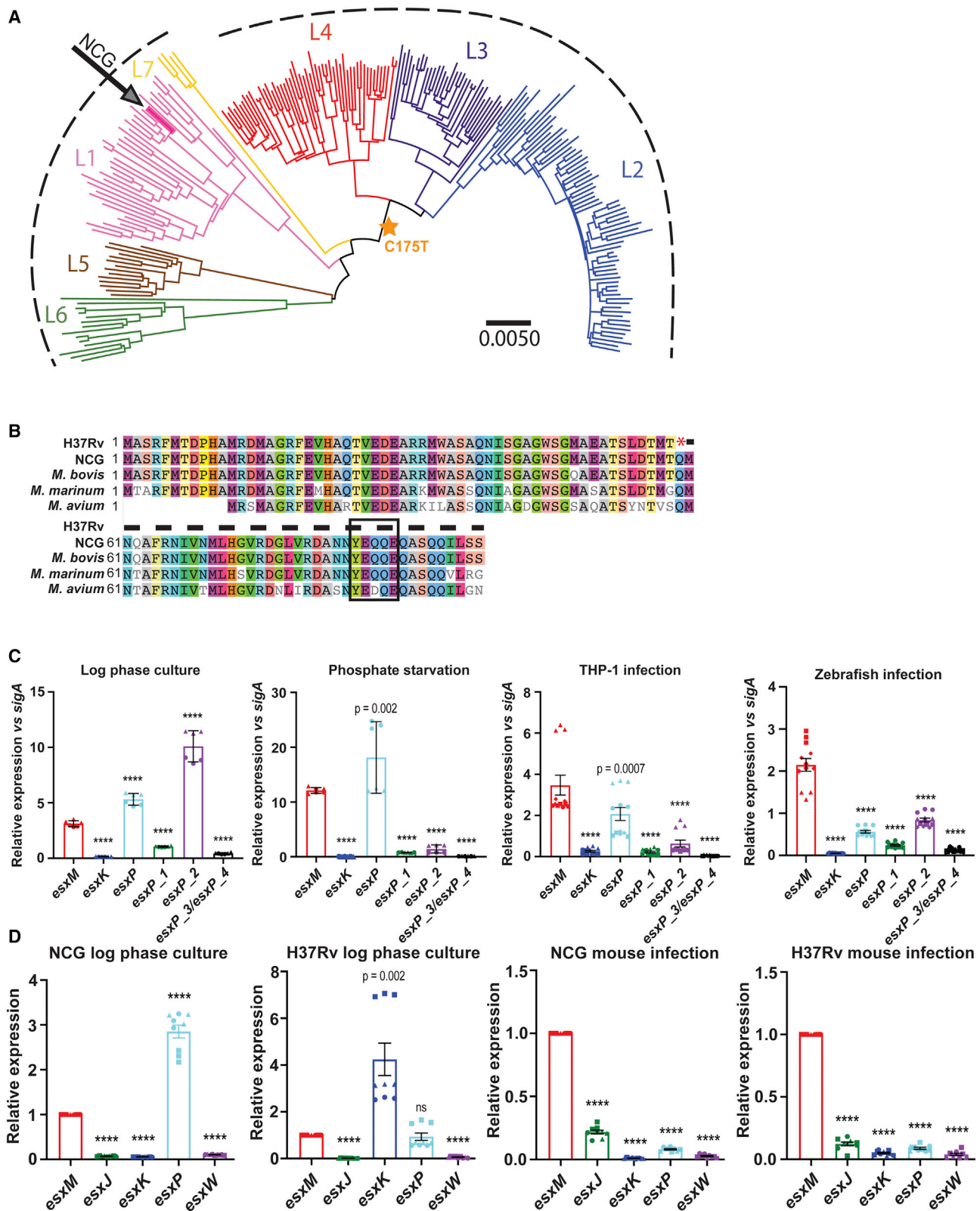
Here, we describe an unusual outbreak of *Mtb* with high rates of extrapulmonary dissemination and bone disease. We uncover a functional variant in the ESX-5 secreted effector EsxM that precisely coincides with a transition from the ancestral allele present

in *Mtb* lineages 1, 5, 6, and 7 to a derived truncation allele in lineages L2–L4. The ancestral version of EsxM present in the outbreak strain, and generally in L1 strains, leads to alterations in the modality of infected host macrophage migration and the rate of egress of infected macrophages from granulomas. *Mtb* generally requires airborne lung-to-lung transmission, so we therefore propose that limiting the degree of dissemination to tissues outside the lung may be advantageous with respect to the likelihood of transmission. We infer that the stop codon in EsxM was introduced in the most recent common ancestor of the L2–L4 *Mtb* strains, leading to decreased rates of dissemination and skeletal disease for strains carrying this variant.

RESULTS

A North Carolina outbreak with high rates of skeletal disease

We investigated a TB outbreak with extremely high rates of disseminated and skeletal disease (Figures 1A and 1B). The index case, a man originally from Vietnam, was diagnosed with pulmonary TB after over a year of symptoms, and a contact investigation was carried out.⁴⁶ Seven secondary cases of active TB were identified (Figures 1A and 1B), and six of the seven (86%) presented with extrapulmonary disease. Remarkably,



(legend on next page)

though the reported frequency of skeletal disease is 2% of all US cases,² four of the extrapulmonary cases (57% of cases in the outbreak) had skeletal disease. The binomial probability of observing four or more bone cases among seven TB patients if the probability of each case having bone TB is equal to the population proportion is approximately 5×10^{-6} . Two of the bone TB cases had a single site of disease in the spine, and the other two had diffuse bony disease involving the ribs, scapula, iliac crest, spine, and sternum (Figures 1C–1E). One of the patients with diffuse bone disease had concurrent pulmonary involvement but no other site, and the other had no site of disease outside the bones. All secondary case patients were US-born (one White, the rest Black), HIV-negative, genetically unrelated to the index case and each other, and seemingly otherwise immunocompetent. The strains isolated from each patient had identical genotypes by mycobacterial interspersed repetitive units-variable number tandem repeats (MIRU-VNTR) typing and spoligotyping, suggesting a single transmitting strain, which we refer to as NCG (Figure S1).

The NCG outbreak strain is a Lineage 1 strain

Extant *Mtb* strains are generally classified by lineage, with so-called “ancestral” strains being from L1, and L5–L7 and so-called “modern” strains being from L2–L4.^{4,47,48} The “modern” lineages are the most prevalent lineages in the Americas, Europe, and parts of Africa and Asia.⁹ Though L1 is responsible for substantial disease burden worldwide, it is comparatively restricted geographically to areas bordering the Indian Ocean; L5–L7 cause the least worldwide burden and are extremely restricted geographically.¹¹ Initial genotyping placed NCG evolutionarily in the Manila clade of L1 (Figure S1A).

After whole genome sequencing, we compared NCG to 37 other L1 strains and identified all NCG-specific variants (Table S1). We did not identify any obvious functional null or gain-of-function variants (structural variants or early stop codons) unique to NCG that would easily explain the clinical phenotype, although it is possible that other variant types contribute to the high rate of bone disease. Given anecdotal reports of higher extrapulmonary dissemination rates overall in “ancestral” lineage strains,^{15,49–52} we considered whether variants shared among multiple, or all, L1 strains might contribute to clinical course.

We first interrogated 225 strains, including NCG, representing multiple strains from each *Mtb* lineage.^{6,53} We called variants

against the L4 H37Rv reference genome and identified 35,787 SNPs across the 225 strains. After removal of genes associated with drug-resistance and those found in repetitive regions of the *Mtb* genome (including PE/PPE and PE-PGRS genes), we used the remaining 31,839 SNPs to construct neighbor-joining and maximum-likelihood phylogenies that placed NCG among L1 strains, confirming the initial genotyping results (Figure 2A).

We next comprehensively assessed lineage- and strain-specific variants across the 225 strains (Table S1). When we compared variants appearing in extant strains from the ancestral lineages (L1, and L5–L7) and modern lineages (L2, L3, and L4), we discovered an ancestral variant present in all L1, and L5–L7 strains (including NCG) in the gene encoding the putative secreted effector EsxM that had not been previously noted as specific to these lineages (Figure 2A and Table S1).

The full-length esxM variant is an ancestral variant specific to a subset of *Mtb* lineages

Like other type VII secretion loci, the ESX-5 locus contains two small Esx proteins encoded in tandem.³⁵ *esxM*, a member of the ~100 amino acid WXG-100 gene family, is located within the ESX-5 locus. It has previously been characterized as a pseudogene in the H37Rv reference genome due to an early stop codon that truncates ~40% of the protein. We found that the “ancestral lineage” *Mtb* strains (L1 and L5–L7), in contrast, contain the complete open reading frame and do not carry the early stop mutation (Figure 2A). The characteristic EsxM truncation identified in “modern” strains (L2–L4) occurs at codon position 59, upstream of the C-terminal regions implicated in secretion.^{55,56}

To replicate these findings in other collections containing L1, we analyzed sequencing data from 3,236 diverse previously published strains from different continents.^{57,58} We found the same association of full-length EsxM with the L1 branch and the truncated variant with the discrete L2–L4 branch (Figures S1B and S1C).

The full-length EsxM variant had previously been reported in one set of clinical strains,⁵⁹ but had not been explicitly associated with the L1 and L5–L7 lineages historically referred to as ancestral. We therefore asked whether the stop-loss variant in EsxM is the ancestral or the derived allele. Other members of the *Mtb* complex such as *Mycobacterium bovis* as well as closely related mycobacterial species, including *Mycobacterium avium* and *M. marinum*, share the stop-loss variant (glutamine residue

Figure 2. Identification of the NCG outbreak strain as a Lineage 1 strain

(A) Whole genome phylogenetic analysis based on reads from Comas et al.,⁶ identifying NCG as a member of the Manila clade of the Lineage 1 (L1) strains. Arrow denotes NCG. Gold star indicates emergence of shared C175T variant common to all L2, L3, and L4 strains. Scale bar indicates substitutions per variant as described in Saelens et al.⁵⁴

(B) Amino acid alignment of EsxM for *Mtb* and other mycobacterial species, noting the early stop codon in modern strains predicted to truncate the protein and eliminate C-terminal secretion sequences (boxed area).

(C) Quantitative RT-PCR analysis showing mean transcript levels of *esxM* and paralogs relative to *sigA* in WT *M. marinum* cultured *in vitro* and upon THP-1 infections (2 dpi) and *in vivo* larval zebrafish (4 dpi) infections. Log phase culture and phosphate starvation—error bars represent SD, data pooled from two independent experiments with three technical replicates for each. THP-1 and *in vivo* infection error bars represent SEM, data pooled from three independent experiments with three technical replicates. One-way ANOVA with Dunnett’s multiple comparisons test.

(D) Mean transcript levels of *esxM* paralogs relative to *esxM* in *Mtb* NCG and H37Rv strains cultured *in vitro* in 7H9 media and upon mouse infection. Bacterial RNA isolated from C57BL/6J mouse lungs at 6 wpi after i.v. infection with *Mtb* NCG or H37Rv strains. Error bars represent SEM, three independent experiments with three technical replicates each. Statistical comparison by one sample t test. ****p < 0.0001.

See also Figures S1 and S2 and Tables S1, S2, and S3.

at amino acid 59) with the ancestral lineage strains of *Mtb*. (Figure 2B). Therefore, we conclude that the full-length EsxM variant is ancestral, and the early-stop variant found in L2–L4 strains of *Mtb* is more recently derived.

Analysis of additional L1 strains reveals an epidemiological association with osteomyelitis

Although not formally tested in large case-control studies, several epidemiological studies, while not definitive, have suggested that L1 strains carrying the ancestral allele present with higher rates of extrapulmonary disease.^{15,49–52} To assess more systematically and in a larger dataset whether there was an association of L1 strains (full-length EsxM) with bone disease, we identified one of the few datasets with whole genome information that includes systematic reporting on osteomyelitis.⁵⁸ The ten-year UK study included over 1,600 patients, with representation of the four most common *Mtb* lineages. Using this dataset, we found that infection with L1 strains (full-length EsxM) was associated with bone disease ($p = 0.0001$, OR 2.5, 95% CI 1.6–4.0) compared to the lineages with the derived *esxM* allele (L2–L4) (Table S2). Thus, we decided to examine the role of the full-length EsxM variant in dissemination and bone disease, as well as the regulation and function of EsxM in both *Mtb* and the closely related pathogen *M. marinum*.

Conserved organization and infection-dependent regulation of the ESX-5 locus in *M. marinum* and *M. tuberculosis*

Though the EsxM variant is a strong candidate for a functional variant due to the early stop codon, we considered whether close ESX-5 paralogs might compensate, leaving the organism functionally unchanged. To test this hypothesis computationally, we calculated if any of the close EsxM paralogs showed a change in their rate of evolution in the modern lineages, which would be consistent with subfunctionalization resulting in little or no overall functional change; however, we did not detect a significant change in the rate of evolution for any of these paralogs (Table S3). Further arguing against this hypothesis of complementation between paralogs is that these paralogous loci are differentially regulated at the transcriptional level,⁶⁰ and mutations result in specific, non-redundant phenotypes in *M. marinum*.⁶¹

M. marinum, a close relative of the *Mtb* complex, encodes full-length EsxM, and, apart from ESX-2, shares orthologous ESX loci with *Mtb*. The *esxM* gene is found within the *M. marinum* ESX-5 locus, and its encoded amino acid sequence is 87% identical to EsxM in the L1 *Mtb* strains.⁶² The principal ESX-5 locus is conserved in both *M. marinum* and *Mtb* and contains the small effectors EsxM and EsxN within a core secretion apparatus.^{41,63} Both *M. marinum* and *Mtb* contain four additional loci encoding small EsxM/N-related proteins that are secreted by the ESX-5 machinery. Consistent with previous analyses,^{41,61} our investigation of synteny and sequence conservation revealed matching homologous regions between *M. marinum* and *Mtb* and closely corresponding EsxM/EsxN-like proteins (Figure S2A).

Because EsxM/EsxN proteins and their paralogs have high levels of sequence homology, we sought to investigate the regulation of these loci in varying contexts, including conditions previously reported to alter ESX-5 transcription in *Mtb*.⁶⁰ We devel-

oped a qRT-PCR-based assay targeting divergent sequences at the 5' end of each *esxM*- and *esxM*-like paralog transcript for *M. marinum* and *Mtb*. In *M. marinum*, we found that although *esxM* was substantially expressed during growth in liquid cultures, two other *esxM*-like transcripts were more abundant (Figure 2C). Upon phosphate starvation, the relative expression of *esxM* increased and was exceeded by only one paralog (Figure 2C). However, EsxM became the clear predominant paralog during infection, both in cell culture and during infection of zebrafish larvae, a natural host (Figure 2C).

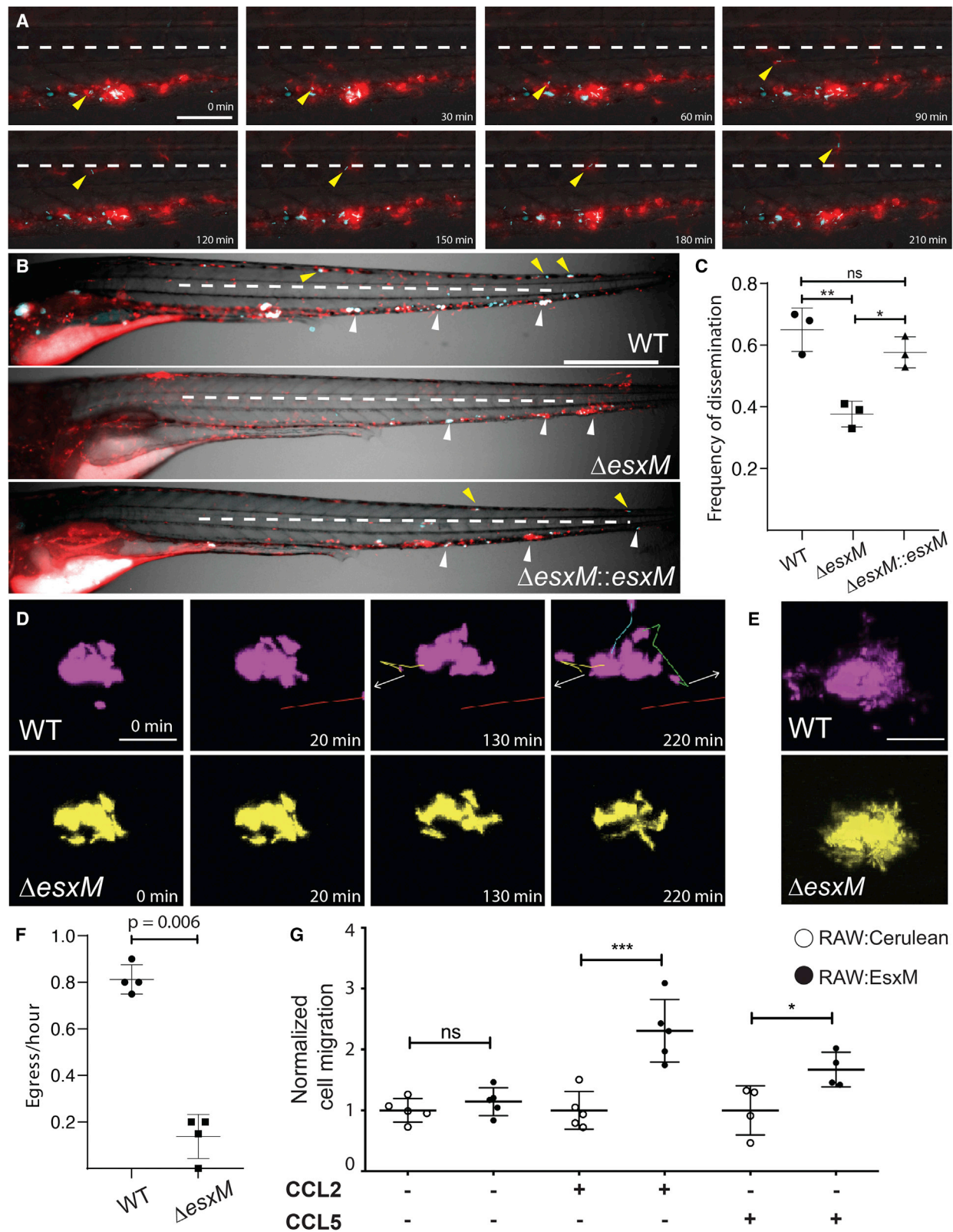
We applied the same strategy to bacterial RNA from *Mtb* to investigate whether infection-dependent upregulation of *esxM* is conserved. We analyzed two *Mtb* strains: H37Rv, a L4 strain containing the early stop codon in EsxM, and the L1 NCG outbreak strain. Paralleling results from *M. marinum*, *esxM* transcript was expressed substantially in broth cultures but was not the most abundant paralog for either strain (Figure 2D). RNA-seq-based analysis of both *Mtb* strains grown in broth validated our qRT-PCR assay, with concordant results in transcript levels between the two assays (Figure S2B).

To test whether *esxM* was differentially regulated during *Mtb* infection, we infected C57Bl/6J mice intravenously (i.v.) with each strain and extracted bacterial RNA from mouse lungs at 6 weeks post-infection. We found that *Mtb* *esxM* became the predominantly expressed paralog during *in vivo* infections, with a dramatic upregulation of the *esxM* transcript (Figure 2D) for both the L1 NCG outbreak strain and the L4 H37Rv strain. These results are also consistent with previously reported cell culture infection experiments using *Mtb*.⁵⁷ Thus, in cell culture, zebrafish, and mouse infections, *esxM* remained the predominant paralog, and hence our top candidate for contributing to the clinical dissemination phenotype.

Characterization of a *M. marinum* *esxM* mutant

In humans, *M. marinum* infections are temperature limited but can often result in tenosynovitis and osteomyelitis.⁶⁴ In zebrafish and other teleosts, *M. marinum* infections can disseminate widely, often with bone involvement.⁶⁵ To test the hypothesis that *esxM* promotes dissemination, we genetically disrupted *esxM* in *M. marinum* to study dissemination, particularly to bone, using the natural zebrafish host.

To first test the impact of EsxM on protein secretion, we grew the WT (full-length EsxM), Δ *esxM*, and the complemented strain (extra-chromosomal expression of *esxM* from the *hsp60* promoter) in Sauton's media *in vitro*. We performed mass spectrometry-based proteomic analysis of the secreted protein fractions. Importantly, the deletion and restoration of EsxM did not have widespread impacts on the *M. marinum* secretome. EsxM itself was only detected in culture filtrates from the complemented (and overexpressed) strain, likely due to low levels of expression and/or regulation of secretion under standard conditions, consistent with the lower levels of transcription we identified in broth-grown cultures (Table S4). However, we were able to detect EsxN, the putative secreted partner of EsxM, from wild-type WT *M. marinum* culture filtrates, and found that deletion of the EsxM partner resulted in the absence of secreted EsxN, a phenotype that was fully complemented upon restoration of EsxM (Figure S2C). In contrast, other ESX-5 substrates were



(legend on next page)

secreted at similar or increased levels in the *esxM* mutants, suggesting that any phenotype observed was specific to EsxM and not an indirect consequence of a general ESX-5 secretion defect (Figure S2C and Table S4).

As additional confirmation that EsxM could be secreted, we examined the expression of a tagged, complementing version of EsxM introduced into WT or *esxM* mutants under both standard and low-phosphate conditions. For both WT and mutant bacterial strains, we observed robust secretion of EsxM, detectable in the culture filtrate under low phosphate conditions (Figures S2D and S2E), an *in vitro* condition under which ESX-5 components are also transcriptionally induced (Figure 2C).⁶⁰

Mutations in *esxM* result in decreased dissemination independent of burden

Early events of mycobacterial infection largely rely on macrophages infected with intracellular bacteria. We first sought to identify dissemination of WT *M. marinum* possessing an intact copy of *esxM* via the egress of infected macrophages from early granulomas, a mechanism by which mycobacteria disseminate within their host.²³ We infected larval zebrafish at 2 days post-fertilization (dpf). Due to the site of infection, most initial granulomas form ventrally. Intravital time-lapse experiments with longitudinal imaging over 15 h between 4 and 5 dpi captured trafficking of infected macrophages from nascent granulomas to sites above the midline, where dorsal granulomas can be established (Figure 3A and Video S1).

To quantitate dissemination to distal points, we measured the rate at which infection spread above the midline (Figure 3A). We found that WT *M. marinum* (EsxM full-length) disseminated to the dorsal side of the larval zebrafish midline in ~70% of samples by 5 days post-infection (dpi) (Figures 3B and 3C). In contrast, Δ *esxM* mutants displayed a 2-fold reduction in dorsal dissemination (Figures 3B and 3C). The mutant could be complemented through constitutive extra-chromosomal expression of *esxM* (Figures 3B and 3C).

We observed no significant difference in bacterial burden in Δ *esxM* at the 5 dpi time point (Figure S3A), indicating that the initial dorsal dissemination phenotype is not a downstream effect of decreased overall burden. We also asked, using a slightly lower starting dose, whether overexpression of *esxM* in a WT *M. marinum* strain could enhance rates of dissemination; we observed a trend toward increased dissemination, although this was not statistically significant (Figure S3B). Overall, these exper-

iments suggest that modulation of bacterial EsxM levels is associated with dissemination of infection to new sites and tissues.

Cell-autonomous effects of EsxM on infected macrophages in granulomas *in vivo*

Although we observed macrophages infected with EsxM-expressing *M. marinum* disseminating at a higher rate, this could arise through non-cell-autonomous effects of EsxM expression—for example, changing the overall inflammatory environment within the granuloma. To address this possibility, we co-infected larval zebrafish with differentially labeled WT and Δ *esxM* *M. marinum* and assessed dissemination from granulomas composed of mixed infected macrophages in equal proportions. Importantly, individual macrophages within the granuloma contained only one strain or the other, enabling testing of cell-autonomous effects. In mixed granulomas, granuloma macrophages infected with Δ *esxM* bacteria egressed at a dramatically lower rate than adjacent macrophages infected with WT *M. marinum* (Figures 3D–3F and Video S2). Thus, the *esxM* macrophage dissemination phenotype appears to be cell autonomous, suggesting local intracellular modulation of the infected host cell.

To assess whether secreted EsxM might directly modulate macrophage-mediated dissemination, we examined whether EsxM expression was sufficient to alter macrophage migration behavior and motility in the absence of any other bacterial proteins or lipids. In cultured mammalian macrophages, we found that cells heterologously expressing full-length EsxM from *Mtb* migrated through transwell membranes across a gradient at a higher rate than control macrophages in the presence of chemokines (Figure 3G).

To investigate macrophage behavior in response to a defined inflammatory stimulus, we performed zebrafish larval tail fin transections and measured recruitment of macrophages to the wound site. To understand the role of full-length EsxM in macrophage migration, we created a set of transgenic zebrafish lines that expressed bacterial EsxM (*M. marinum* EsxM, codon optimized for expression in zebrafish) from a macrophage-specific promoter (*Tg(mfap4:esxM-p2a-tdTomato^{xt49})*) (Figures 4A and 4B). Macrophages producing EsxM arrived at the wound after tail transection much faster and in greater numbers than control macrophages from a matched macrophage transgenic line expressing only the fluorophore (Figures 4C–4E and Video S3). We also found that *esxM*-expressing macrophages demonstrated an elevated maximum migration velocity compared to

Figure 3. Dissemination *in vivo* is dependent on *esxM*

- (A) A macrophage infected with WT *M. marinum* departs from an early granuloma and migrates above the midline (dashed white line). Scale bar, 50 μ m.
(B) Representative images from WT *M. marinum*, Δ *esxM*, and Δ *esxM*:*esxM* infections in larval zebrafish. 2 dpf zebrafish with red fluorescent macrophages are infected ventrally in the caudal vein with cerulean-expressing *M. marinum*. Scale bar, 500 μ m.
(C) At 5 dpi, Δ *esxM* demonstrates a reduced frequency in dissemination above the midline (white dashed line) to the dorsal side of the animal adjusting for burden across all three groups. One-way ANOVA with Tukey's post-test, data from three biological replicates, mean \pm SD shown. $n > 35$ /experiment.
(D) Co-infection with WT and Δ *esxM* *M. marinum* results in larval granulomas populated by both strains. Time-lapse imaging reveals WT *M. marinum* egressing from the granuloma (tracking lines), while Δ *esxM* remains confined within. White arrows indicate direction of egress. Scale bar, 50 μ m.
(E) Projection of time-lapse imaging in (D) showing complete range of movement for macrophages infected with each strain over 220 min; Scale bar 50 μ m.
(F) Quantification of rate of egress for WT and Δ *esxM* *M. marinum* from co-populated granulomas. Long-term monitoring of 4 mixed granulomas from 4 independent animals. Student's paired t test, mean \pm SD shown.
(G) Migration of RAW 264.7 cells expressing fluorescent cerulean control or EsxM through transwell membranes in the presence and absence of chemokine. One-way ANOVA with Bonferroni's post-test. * $p < 0.05$, ** $p < 0.01$, *** $p < 0.001$.
See also Figure S3, Table S4, and Videos S1 and S2.

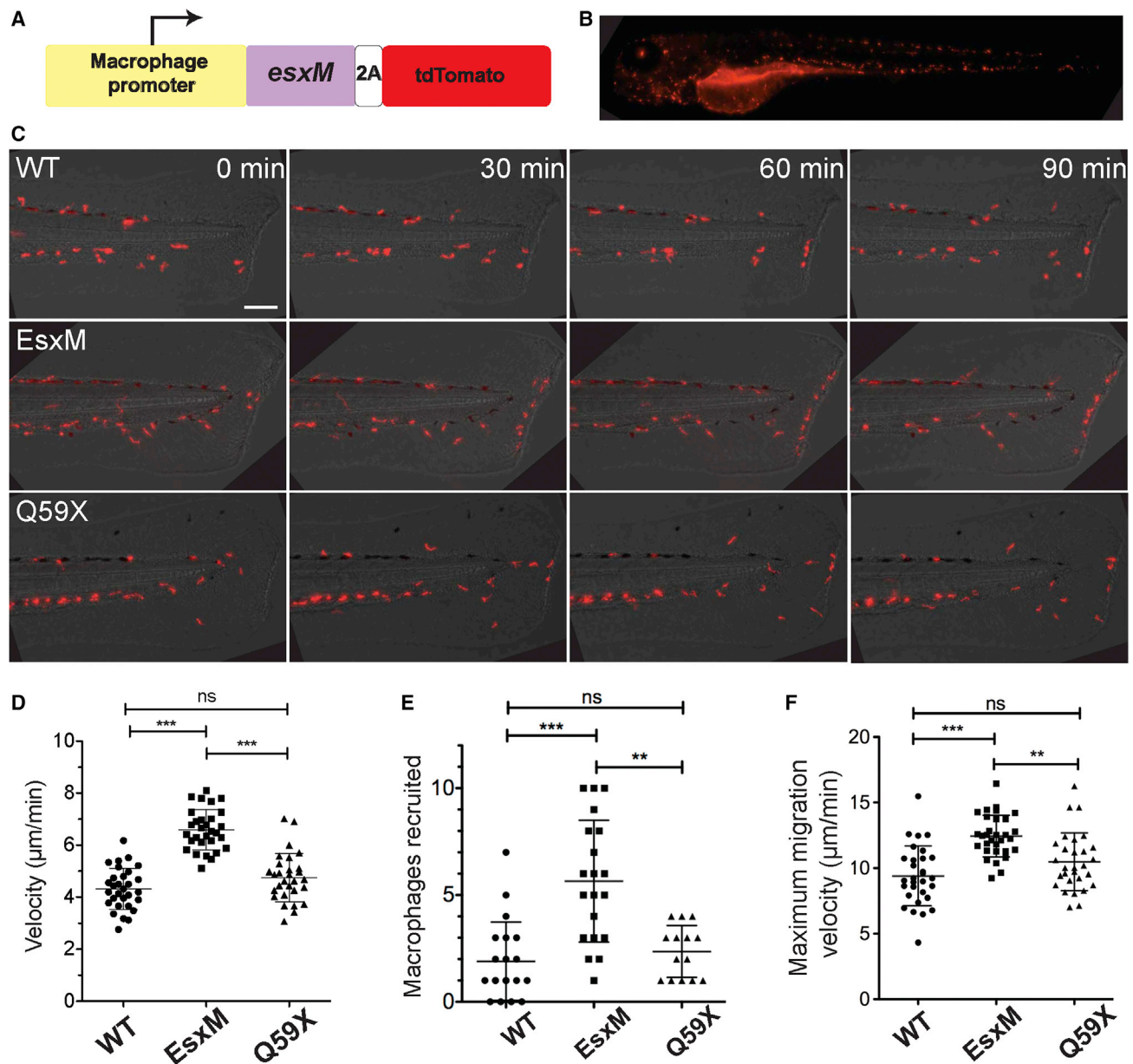


Figure 4. Macrophage-specific expression of ancestral full-length EsxM, but not its paralogs or modern, truncated EsxM, alters macrophage motility

(A) Transgene design (not to scale) for macrophage-specific expression of EsxM. The macrophage-specific zebrafish promoter *mfap4* drives expression of the mycobacterial protein within zebrafish macrophages. 2A peptide uncouples EsxM protein (98 AA) from tdTomato.

(B) Representative larval zebrafish expressing the *mfap4:esxM-p2A-tdTomato* transgene. Scale bar, 500 μm .

(C) Increased macrophage motility in the absence of infection for EsxM-expressing transgenic zebrafish lines. Scale bar, 100 μm .

(D) Migration and velocity measured in response to tail fin transection. One-way ANOVA, Dunn's multiple comparison test. Data representative of three biological replicates.

(E) Number of macrophages recruited to tail wound 90 min post-transection. Macrophages express fluorescent TdTomato, EsxM, or truncated EsxM (Q59X) via a macrophage-specific promoter (*mfap4*). One-way ANOVA with Dunn's multiple comparison test. Data representative of three biological replicates.

(F) Maximum velocity of macrophages migrating to tail wound. One-way ANOVA with Dunn's multiple comparison test. Data representative of three biological replicates. Mean \pm SD shown on all graphs. ** $p < 0.01$, *** $p < 0.001$.

See also Figure S3 and Video S3.

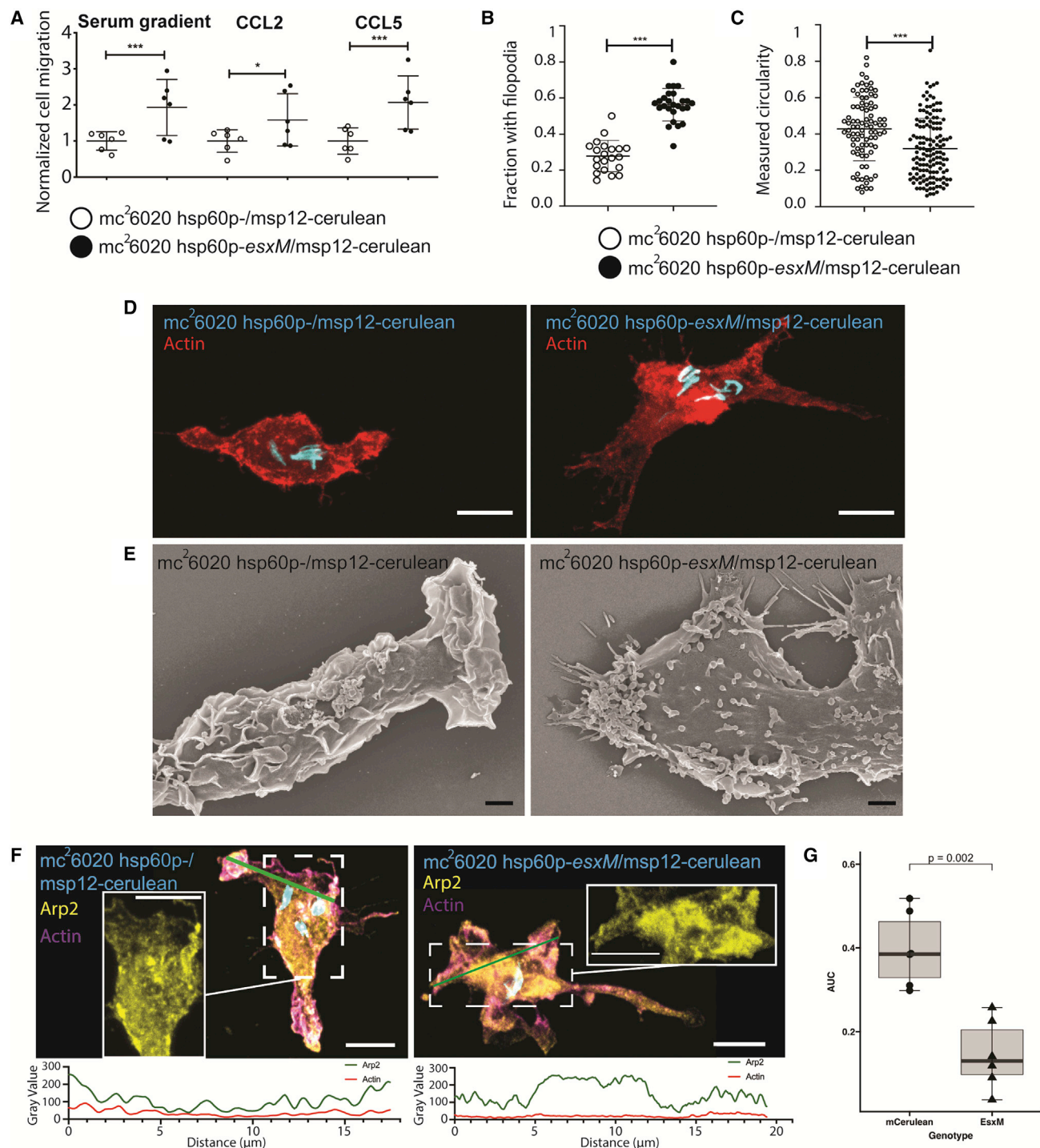


Figure 5. Reintroduction of ancestral EsxM into modern *Mtb* reprograms macrophage motility through cytoskeletal alterations

(A) RAW264.7 cell migration during infection with *Mtb* strains *mc*²6020 (*Mtb*₆₀₂₀ *msp12*:cerulean) or *mc*²6020 constitutively expressing *esxM* (*Mtb*₆₀₂₀ *hsp60p*:*esxM*/*msp12*:cerulean) from an episomal plasmid across transwell membranes in the presence and absence of chemokine. Mean ± SD shown. One-way ANOVA with Bonferroni's correction.

(B) Quantitation of the presence of filopodia on BLAER1 cells infected with *Mtb*₆₀₂₀ *msp12*:cerulean or *Mtb*₆₀₂₀ *hsp60p*:*esxM*/*msp12*:cerulean. Two-tailed paired Student's *t* test, mean ± SD shown.

(C) Measured circularity of BLAER1 cells infected with *Mtb*₆₀₂₀ *msp12*:cerulean or *Mtb*₆₀₂₀ *hsp60p*:*esxM*/*msp12*:cerulean.

(legend continued on next page)

control macrophages (Figure 4F). As an additional control, we generated a transgenic line that drove macrophage-specific expression of the truncated EsxM found in modern lineages of *Mtb* (*Tg(mfap4:esxM_Q59X-p2a-tdTomato^{xt50})*). These macrophages behaved similarly to controls (Figures 4C–4F and Video S3). As a control for the function of other ESX-secreted proteins, we created a transgenic line in which the paralogous protein EsxB from the ESX-1 locus was driven in macrophages (*Tg(mfap4:esxB-p2a-mNeonGreen^{xt51})*). EsxB-expressing macrophages were indistinguishable from WT macrophages in these assays (Figures S3C and S3D).

We returned to our mixed granuloma model to assess the effects of EsxM on macrophage motility in a natural infection. We assayed the velocity of zebrafish macrophages infected with WT or Δ esxM *M. marinum* as they departed granulomas. Δ esxM-infected macrophages departed established granulomas at a much lower rate overall, and the subset of Δ esxM-infected macrophages that did depart migrated at a lower velocity (Figures 3D and S3E). Overall, a strikingly low number of Δ esxM-infected macrophages departed established granulomas in the mixed infection experiments (Figure 3D).

To gain further insight into the observed cell-autonomous effect of EsxM on migration velocity, we measured the migration velocity of infected macrophages not in granulomas during the mixed infection. Here, we also observed a significant decrease in the migrating velocity of Δ esxM-infected macrophages compared to those infected with WT *M. marinum*, despite an overall higher rate of migration velocity relative to macrophages within granulomas (Figure S3F). Together, these results suggest that full-length EsxM is both required and sufficient for characteristic alterations in macrophage behavior, including egress from the initial granulomas that form during infection.

Reconstitution of ancestral EsxM in an attenuated modern *Mtb* strain enhances macrophage motility

We next determined whether EsxM could enhance the migratory behavior of its primary host cell type in the context of infection with *Mtb*. We reconstituted the ancestral protein in an attenuated modern L4 *Mtb* strain. Using mc²6020, a double deletion (Δ lysA Δ panCD) auxotrophic mutant from the H37Rv background⁶⁶ (i.e., a strain of *Mtb* that harbors the derived Q59X allele in *esxM*), we investigated whether expression of the ancestral, full-length *esxM* in *Mtb* enhances the migratory capacity of infected macrophages. We found that RAW 264.7 macrophages infected with full-length *esxM*-expressing mc²6020 migrated directionally in a transwell assay at a higher rate than cells infected

with control mc²6020, both in a serum gradient and in the presence of chemokines (Figure 5A). These results indicate that full-length, ancestral *esxM* expressed in a L4 *Mtb* strain promotes mammalian host cell migration during *Mtb* infection. During these experiments, we observed that the ancestral EsxM-expressing strain induced a distinct morphology of the infected macrophages compared to control infections, with the emergence of increased numbers of membrane spikes resembling filopodia (Figure S4A).

To explore this phenotype further in a human cell line, we used BLAER1 cells that, after transdifferentiation into macrophage-like cells, recapitulate critical aspects of macrophage biology.^{67,68} We infected transdifferentiated BLAER1 cells with *Mtb* strain mc²6020 with a plasmid expressing cerulean fluorescent protein or an identical plasmid expressing cerulean fluorescent protein and ancestral *esxM*. Similar to the result in RAW 264.7 cells, infection of the human macrophage cell line with *Mtb* expressing ancestral EsxM resulted in increased filopodial protrusions (Figures 5B and 5D). In addition, transdifferentiated BLAER1 cells infected with *Mtb* expressing ancestral EsxM took on a more extended morphology relative to those infected with the control *Mtb* strain (Figures 5C and 5D).

To characterize EsxM-dependent macrophage alterations more fully, we performed electron microscopy on infected macrophages from the *Mtb* mc²6020 strain with the control plasmid or the mc²6020 strain expressing ancestral, full-length EsxM. We found dramatic differences at the macrophage surfaces. Macrophages infected with the control strain had easily recognizable lamellipodia and prominent membrane ruffling, whereas those infected with *Mtb* expressing ancestral EsxM instead displayed prominent filopodia and extensive membrane blebs at the edge of the infected macrophage (Figure 5E).

These alterations closely resembled those described for a macrophage-specific knockout of *Arpc2* in mouse macrophages.⁶⁹ In addition, *Arpc2*^{−/−} macrophages, under some conditions, display increased random migration speeds as well as increased velocities during migration to chemoattractants.⁶⁹ We therefore asked whether EsxM expression may disrupt this pathway, leading to the observed *Arpc2*-like phenotype in terms of increased migration and altered morphology (Figures 5A and 5F). Though Arp2 localizes to the periphery of macrophages infected with the modern *Mtb* strain, there is consistent disruption of Arp2 localization in macrophages infected with *Mtb* expressing full-length EsxM, with Arp2 confined to the interior (Figures 5F, 5G, S4B and S4C). In addition, treatment of zebrafish larvae with Arp2/3 inhibitor CK66^{70,71} pharmacologically rescued the decreased migration velocity of

(D) BLAER1 cells infected with *Mtb*₆₀₂₀ *hsp60p::esxM/msp12::cerulean* demonstrate increased filopodia and reduced circularity compared to BLAER1 cells infected with *Mtb*₆₀₂₀ *msp12::cerulean*. Bacteria in cyan and actin in red. Scale bar, 8 μ m.

(E) Electron micrographs of BLAER1 cells infected with *Mtb*₆₀₂₀ *hsp60p::esxM/msp12::cerulean* demonstrate increased filopodia compared to BLAER1 cells infected with *Mtb*₆₀₂₀ *msp12::cerulean*. Scale bar, 2 μ m.

(F) BLAER1 cells infected with *Mtb*₆₀₂₀ *msp12::cerulean* demonstrate peripheral localization of Arp2, compared to interior localization of Arp2 in cells infected with *Mtb*₆₀₂₀ *hsp60p::esxM/msp12::cerulean*. Insets display fluorescence intensity of Arp2 and actin along the green line, with interior localization in *Mtb*₆₀₂₀ *hsp60p::esxM/msp12::cerulean* infections.

(G) Quantification of Arp2 localization from (F). Plot of the percentage of the area under the curve (AUC) for fluorescence in the Arp2 channel for the interval 0% to 25% of the normalized distance across the longest cell axis normalized to AUC from the middle 50% (25%–75%) of the total cell length. Each data point represents a single cell. Statistics from Student's *t* test. Scale bar, 8 μ m. **p* < 0.05, ***p* < 0.01, ****p* < 0.001.

All images are representative of at least two biologically independent experiments.

See also Figure S4.

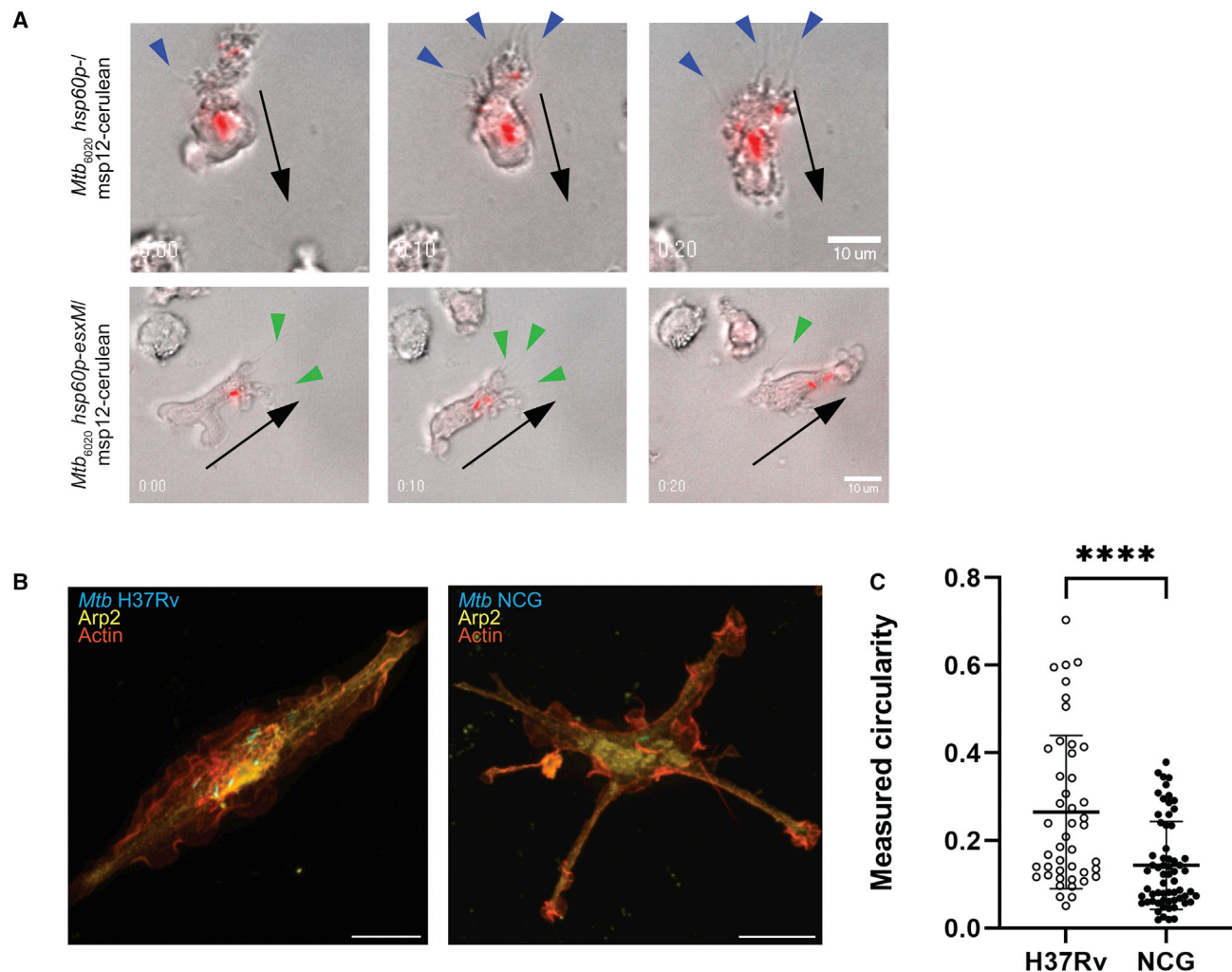


Figure 6. Altered macrophage motility and morphology during *M. tuberculosis* infection with full-length EsxM variants

(A) Time-lapse imaging of BLAER1 cells infected with *Mtb₆₀₂₀ msp12::cerulean* or *Mtb₆₀₂₀ hsp60p::esxM/msp12::cerulean*. Bacteria false-colored red. Spiky projections, likely retraction fibers, (blue arrowheads) localize to the lagging edge in BLAER1 cells infected with *Mtb₆₀₂₀ msp12::cerulean*. Filopodial projections (green arrowheads) localize to the leading edge in BLAER1 cells infected with *Mtb₆₀₂₀ hsp60p::esxM/msp12::cerulean*. Black arrows indicate the direction of cell migration.

(B and C) Infection of BLAER1 cells with Lineage 4 (L4) *Mtb* H37Rv results in infected cells with membrane ruffles. Infection with the Lineage 1 (L1) *Mtb* NCG outbreak strain results in an increase in spiky projections and (C) a decrease in circularity, two-tailed paired Student's *t* test, mean \pm SD shown. *****p* < 0.0001. All images representative from at least two biologically independent experiments.

See also Figures S4 and S5 and Video S4.

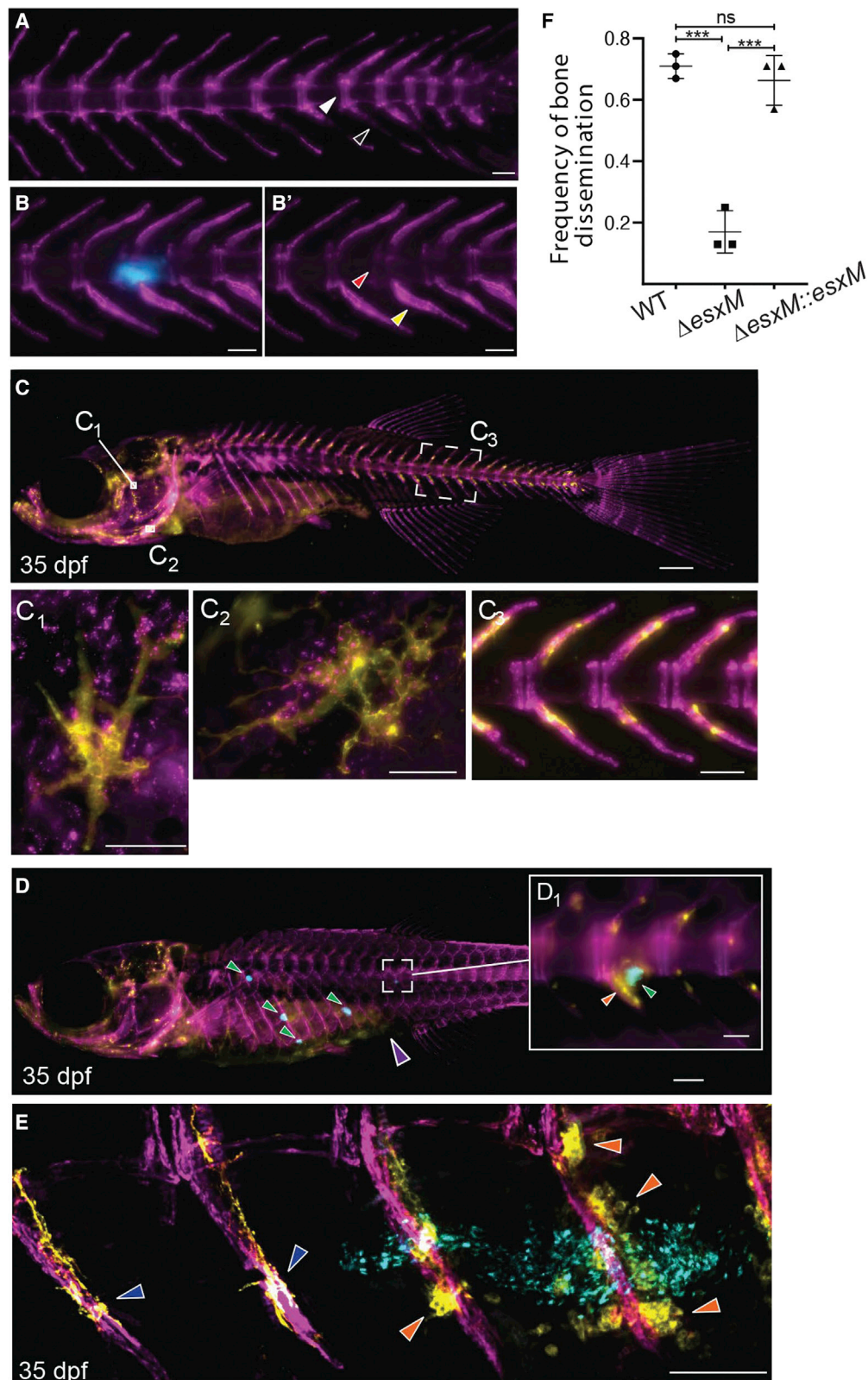
Δ esxM-infected macrophages, indicating that EsxM may regulate the host cytoskeletal axis *in vivo* (Figure S5 and Video S4).

To examine how the differences we observed influence migration, we performed live imaging of transdifferentiated BLAER1 macrophages infected with the two *Mtb* strains that differ only in the expression of full-length EsxM. The leading edge of macrophages infected with the control *Mtb* strain displayed classical lamellipodia and ruffles that predicted the direction of movement (Figure 6A). In contrast, prominent filopodial projections marked the leading edge of the cells infected with *Mtb* expressing ancestral EsxM (Figure 6A). Thus, ancestral EsxM is required and sufficient in a variety of contexts to alter macrophage migratory dynamics and subsequent mycobacterial dissemination.

To confirm that the reconstitution experiments reflect the biology of the outbreak strain itself, we performed BLAER1 macrophage infections with cerulean-labeled versions of the L4 strain H37Rv and the NCG outbreak strain. Although we were not able to perform macrophage motility assays under BSL3 conditions, we found that cells infected with the NCG strain displayed similar alterations in morphology, with more extended branches than H37Rv-infected cells (Figures 6B, 6C, and S4D).

Ancestral esxM promotes dissemination to bone *in vivo*

We next explored *in vivo* whether this altered macrophage motility might contribute to the outbreak's clinical phenotype



(legend on next page)

using a zebrafish infection model.^{72,73} Like human bone, zebrafish bone consists of osteocytes, bone-lining cells, osteoblasts, and mono- and multinucleate osteoclasts.⁷⁴ Key signaling molecules that regulate bone-remodeling cells are conserved between humans and zebrafish.^{72,75} Human genetic variants affecting bone physiology and development have translated into similar alterations in zebrafish bone.^{76–80}

In cases of TB skeletal disease in humans, the spine is the most common site of infection.⁸¹ Likewise, spinal deformities in zebrafish have long been known to be a sign of mycobacterial infection in aquaculture.⁶⁵ We infected the osteoblast reporter line *Tg(Ola.Sp7:mCherry-Eco.NfsB)^{pd46}* and examined *M. marinum*-induced pathology in zebrafish bone. Periostitis and lytic lesions are a well-documented consequence of skeletal TB in humans.⁸² We found that infection with *M. marinum* led to an increased signal from osteoblasts near sites of *M. marinum* infection and erosion of bone in contact with mycobacterial infection (Figure 7A–7B').

We next developed an osteoclast-specific transgenic line using upstream regulatory sequences of the zebrafish tartrate-resistant acid phosphatase gene (*Tg(acp5a:mNeonGreen-CAAX)^{xt52}*), which labeled osteoclasts specifically (Figure 7C). Using a dual osteoblast-osteoclast transgenic line derived from crossing the two lines, we infected zebrafish at 3 weeks post-fertilization (wpf) and traced the dissemination of *M. marinum* to skeletal sites two weeks later (Figures 7D and 7E). We found consistent and substantial dissemination of infection to bone at this time point (Figures 7D–7F). At sites of spinal infections in juvenile zebrafish, we noted a strong response by proximal osteoclasts and osteoblasts alike. Osteoclasts near *M. marinum* appeared in greater number and altered morphology (Figure 7E). Despite the close developmental relationship between macrophages and osteoclasts, we did not find any evidence of osteoclasts infected with *M. marinum*.

Finally, we infected juvenile zebrafish intraperitoneally with WT, Δ esxM, and the complemented mutant at 3 wpf and assessed the presence of spinal infections at 2 weeks post-infection (wpi). Although juvenile zebrafish infected with WT *M. marinum* developed spinal infections in ~70% of samples by 2 wpi, this proportion was reduced to ~20% in Δ esxM infec-

tions (Figures 7D–7F). The mutant could be complemented through constitutive extra-chromosomal expression of *esxM* (Figures 7D–7F).

DISCUSSION

Investigation of outbreak strains with extreme phenotypes can lead to mechanistic understanding of critical host-pathogen interactions that promote or restrain virulence and transmission. Here, we link an unusual *Mtb* outbreak with high rates of dissemination and skeletal disease to a specific *Mtb*-secreted effector that is present in the so-called “ancestral” lineages but truncated in major *Mtb* lineages L2–L4, the most broadly distributed lineages geographically.

Full-length EsxM is both necessary and sufficient to drive *in vivo* changes in the motility of infected macrophages, rates of granuloma egress and dissemination, and ultimately interaction with bone. Notably, reintroduction of the full-length EsxM into a modern *Mtb* strain resulted in a change in the migration modality of infected macrophages. Generally, lamellipodia at the leading edge are associated with macrophage migration within interstitial tissues.⁸³ In cells infected with an *Mtb* strain expressing reconstituted ancestral EsxM, a dramatic reprogramming of macrophage motility occurred, from lamellipodia-led migration to motility marked by filopodia at the leading edge and membrane blebbing. We hypothesize that ancestral and generalist mycobacterial pathogens benefit from dissemination via enhanced macrophage motility, and that the derived truncation of EsxM in L2–L4 curtails overall dissemination to some degree.

Our finding that the L2–L4 *Mtb* strains contain a derived, truncated version of EsxM suggests its functional change would have significantly altered their properties during human infection. Infection of non-transmissible tissue sites such as bone would not promote transmission.⁸⁴ Inversely, mutations that increase the likelihood of spreading to new hosts would be selected for, provided there is a sufficiently large host population and therefore may influence the transmission dynamics of these strains.⁸⁵ The derived EsxM variant may shape the properties of *Mtb* strains from L2–L4, perhaps by promoting residence in the lungs,

Figure 7. Ancestral *esxM* promotes spinal dissemination

- (A) Representative image of sham-injected osteoblast line 3 weeks post-injection. Intervertebral spacing is tightly delineated (white arrowhead), and osteoblast signal at hemal arches is typical of healthy zebrafish (black arrowhead). Scale bar, 500 μ m.
- (B) Representative image of cerulean *M. marinum*-infected osteoblast line, three weeks post-infection (wpi) showing bone-associated infection. Scale bar, 100 μ m.
- (B') Same animal as in (B), showing only osteoblasts. *M. marinum* has invaded into the intervertebral space, giving rise to a vertebral lesion (red arrowhead) and proliferation of osteoblasts proximal to infection (yellow arrowhead). Scale bar, 100 μ m.
- (C) Dual transgenic line at 35 dpf labeling osteoblasts in purple from the *Sp7/osterix* promoter and osteoclasts from the *acp5a*/TRAP promoter in yellow. Scale bar, 500 μ m.
- (C₁–C₃) Insets show tight association of osteoblasts and osteoclasts along the spine (C₃). Yellow multinucleate osteoclasts are also visible in the head (C₁ and C₂). C₁ inset scale bar, 500 μ m C₂ inset scale bar, 50 μ m. C₃ inset scale bar, 100 μ m.
- (D) Intraperitoneal infection of juvenile animals with cerulean-fluorescent *M. marinum* results in frequent dissemination to spine (approximately 70% of animals). Scale bar, 500 μ m.
- (D₁) High magnification view of boxed area of (D) showing association of granuloma with spine and alterations in normal osteoclast distribution. Scale bar, 100 μ m.
- (E) PACT-based clearing techniques in adults and juveniles enable high-resolution imaging of sites of bone disease. Confocal image of dorsal region of spine showing unaffected vertebrae with typical osteoclast behavior (dark blue arrowheads) and altered osteoclast behavior (orange arrowheads) in segments associated with granulomas (bacteria in cyan). Scale bar, 100 μ m.
- (F) Quantitation of dissemination to spine at 14 dpi in intraperitoneal infections. $n \geq 7$ per group for 3 biological replicates. One-way ANOVA with Tukey's post-test, data from three biological replicates, mean \pm SD shown. *** $p < 0.001$.

the site of disease most effective for transmission, and reducing the frequency of unproductive dissemination. Nevertheless, L1 strains remain prevalent in areas bordering the Indian Ocean and may indeed be well adapted to their particular niche or host population,¹¹ and it is notable that the outbreak with high rates of bone disease occurred among a host population where L1 strains are rare. Host genetic variants may also influence the rates of extrapulmonary and skeletal disease.^{86,87}

We identified two large-scale studies with mixed strain populations consisting of L1–L4; one in Vietnam and one in Birmingham, UK.^{57,58} The Vietnamese dataset did not include any information about rates of osteomyelitis, but both studies suggested a substantial transmission advantage for the lineages that had the derived, truncated *EsxM* allele over the full-length allele,^{57,58} at least in these settings. Overall prevalence of the different lineages as well as the emergence and expansion of specific sub-lineages may be driven by genetic lineage and strain-specific factors, but may also be influenced by human migration patterns, changes in ecological niche, or epidemic dynamics over time.^{11,88–90}

The Birmingham, UK study, one of the few large-scale published studies to include detailed information about TB bone disease combined with whole genome sequencing, revealed an additional association of L1 with higher rates of bone disease.⁵⁸ Infection with the modern L2–L4 strains can certainly still result in bone disease,^{91,92} but in the Birmingham study, osteomyelitis occurs at substantially lower rates for the L2–L4 strains carrying the derived *EsxM* truncation than for the Lineage 1 strains with the ancestral allele.

Some additional properties of L2–L4 strains relative to L1 strains are likely attributable to a characteristic deletion present in L2–L4 strains associated with resistance to oxidative stress and hypoxia.¹⁰ Our data reveal that the emergence of *Mtb* L2–L4, the lineages that are most broadly distributed globally, was also marked by an inactivating mutation in *esxM*. We find that the ancestral version of this protein present in L1, and L5–L7 strains, as well as almost all pathogenic mycobacterial species, enhances macrophage motility—reprogramming macrophage migration in infected cells—and promotes dissemination. Results analyzing intrahost strain evolution from human autopsy studies have suggested similar patterns of intra-lung spread and inter-organ spread, indicating that there may be shared dissemination mechanisms, including macrophage trafficking.^{93,94} Although numerous sequence variants separate the *Mtb* lineages, acquisition of the derived *esxM* variant may have contributed to the specialization of L2–L4 to their current human niches and to the clinical properties and progression of infections with these strains.

Limitations of the study

Though we identified a strong association between the full-length ancestral *esxM* allele and bone disease and identified a functional role for this effector using animal models, there are likely other bacterial variants or host factors that contribute to the extremely high rates of bone disease in the North Carolina outbreak. In addition, the *in vivo* regulation of the ESX-5 small, secreted proteins is complex. *esxM* becomes the predominant transcribed paralog in cell culture and animal models of infec-

tion, both in *M. marinum* and *Mtb*, but our evolutionary analysis also revealed strong conservation of other *esxM* paralogs (Table S3) compared to published whole genome analysis of the overall rate of *Mtb* evolution.^{48,95} The roles of these paralogs during mycobacterial growth and pathogenesis remain to be defined. Additionally, although the zebrafish model recapitulates many important aspects of bone disease and dissemination, there are limited mammalian models in which bone dissemination has been established and can be studied.⁹⁶ Finally, the distinction between dissemination and bone tropism remains an open question, as well as the precise nature of the *in vivo* initiation event for the bone-associated granulomas we observe.

STAR★METHODS

Detailed methods are provided in the online version of this paper and include the following:

- **KEY RESOURCES TABLE**
- **RESOURCE AVAILABILITY**
 - Lead contact
 - Materials availability
 - Data and code availability
- **EXPERIMENTAL MODEL AND SUBJECT DETAILS**
 - Ethics statement
 - Human subjects
 - Zebrafish husbandry
 - Zebrafish lines
 - Mice
- **METHOD DETAILS**
 - Mouse infections
 - Larval and juvenile zebrafish infections
 - PACT clearing of juvenile zebrafish
 - Wound recruitment assays
 - Zebrafish drug treatment
 - Generation of transgenic constructs
 - Generation of transgenic zebrafish lines
 - RAW 264.7 transwell migration assays
 - RAW 264.7 transduction
 - THP-1 macrophage infection
 - BLaER1 cell transdifferentiation and infection
 - Scanning electron microscopy
 - BSL3 infections and analysis using *M. tuberculosis* NCG and H37Rv strains
 - Bacterial strains
 - Construction of plasmids
 - Generating the *esxM* deletion in *M. marinum*
 - Protein secretion assays
 - Proteomics
 - RNA isolation and quantitative RT-PCR analysis
 - Protein secretion assay and western blotting
- **QUANTIFICATION AND STATISTICAL ANALYSIS**
 - RNA sequencing of *M. tuberculosis* bacterial transcripts
 - Genome assembly and variant calling
 - Phylogenetic methods
 - In silico analyses
 - Microscopy

- Fiji/ImageJ
- Mass spectrometry statistical analysis

SUPPLEMENTAL INFORMATION

Supplemental information can be found online at <https://doi.org/10.1016/j.cell.2022.10.019>.

ACKNOWLEDGMENTS

We thank R. Asrican, R. Beerman, M. Braunstein, L. Cameron, L. Dolat, Y. Gao, S. Harris, E. Hunt, R. Meade, S. Miller, K. Murphy, C. Pyle, R. Vancini, and C. Xander for experimental advice and assistance; E. Hunt, I. Padmanaban, and A. Yu for zebrafish care; T. Graf for BLER1 cells; M. Bagnat, J. Bear, T. Iorger, D. Pickup, M. Welch, and members of the Tobin laboratory for helpful discussions; and M. Cronan and L. Dolat for comments on the manuscript. Graphical abstract created in part with BioRender. This work was funded by National Institutes of Health grants AI125517 (D.M.T., J.E.S., and S.L.), AI130236, AI127115 (D.M.T.), AI142127, AI149147, AI106872 (P.A.C.), Whitehead Scholar Awards (C.B.L. and C.M.S.), an NIH Director's New Innovator Award 1DP2-GM146458-01 (C.M.S.), and a Vallee Scholar Award (D.M.T.). Biocontainment work performed in the Duke Regional Biocontainment Laboratory received partial support for construction from NIAID (UC6-AI058607).

AUTHOR CONTRIBUTIONS

J.W.S., S.L., J.E.S., and D.M.T. conceived and designed the project; J.W.S., M.I.S., and G.V. performed and analyzed all zebrafish experiments; M.I.S., A.M.X.-M., E.J.H., and C.M.S. performed mouse experiments; G.V. performed bacterial expression analysis; J.W.S., W.J.B., D.M.T., and C.B.L. analyzed publicly available sequence data; W.J.B. and M.I.S. analyzed RNA-seq data; D.M.S. and K.L.J.S. isolated and grew the outbreak strain; A.M.X.-M. performed infection experiments and migration assays; D.D.H., R.M.C., M.M.C., and P.A.C. performed and analyzed proteomic experiments; J.C. supervised BLER1 cell assays; C.M.S. designed and supervised mouse infection experiments; J.W.S., M.I.S., and D.M.T. wrote the manuscript with substantial contributions by G.V. and additional input from all authors.

DECLARATION OF INTERESTS

The authors declare no competing interests.

Received: November 18, 2021

Revised: August 27, 2022

Accepted: October 16, 2022

Published: November 9, 2022

REFERENCES

- World Health Organization (2021). Global Tuberculosis Report 2021 (World Health Organization). <https://www.who.int/publications/i/item/9789240037021>.
- Centers for Disease Control and Prevention (CDC) (2021). Reported Tuberculosis in the United States, 2020 (CDC: US Department of Health and Human Services).
- Crubezy, E., Ludes, B., Poveda, J.D., Clayton, J., Crouau-Roy, B., and Montagnon, D. (1998). Identification of *Mycobacterium* DNA in an Egyptian Pott's disease of 5, 400 years old. *Comptes rendus de l'Académie des sciences. Serie III, Sciences de la vie* 321, 941–951. [https://doi.org/10.1016/s0764-4469\(99\)80009-2](https://doi.org/10.1016/s0764-4469(99)80009-2).
- Brosch, R., Gordon, S.V., Marmiesse, M., Brodin, P., Buchrieser, C., Eiglmeyer, K., Garnier, T., Gutierrez, C., Hewinson, G., Kremer, K., et al. (2002). A new evolutionary scenario for the *Mycobacterium tuberculosis* complex. *Proc. Natl. Acad. Sci. USA* 99, 3684–3689. <https://doi.org/10.1073/pnas.052548299>.
- Orgeur, M., and Brosch, R. (2018). Evolution of virulence in the *Mycobacterium tuberculosis* complex. *Curr. Opin. Microbiol.* 41, 68–75. <https://doi.org/10.1016/j.mib.2017.11.021>.
- Comas, I., Coscolla, M., Luo, T., Borrell, S., Holt, K.E., Kato-Maeda, M., Parkhill, J., Malla, B., Berg, S., Thwaites, G., et al. (2013). Out-of-Africa migration and Neolithic coexpansion of *Mycobacterium tuberculosis* with modern humans. *Nat. Genet.* 45, 1176–1182. <https://doi.org/10.1038/ng.2744>.
- Pepperell, C.S. (2022). Evolution of Tuberculosis Pathogenesis. *Annu. Rev. Microbiol.* 76, 661–680. <https://doi.org/10.1146/annurev-micro-121321-093031>.
- Supply, P., Marceau, M., Mangenot, S., Roche, D., Rouanet, C., Khanna, V., Majlessi, L., Criscuolo, A., Tap, J., Pawlik, A., et al. (2013). Genomic analysis of smooth tubercle bacilli provides insights into ancestry and pathoadaptation of *Mycobacterium tuberculosis*. *Nat. Genet.* 45, 172–179. <https://doi.org/10.1038/ng.2517>.
- Gagneux, S., and Small, P.M. (2007). Global phylogeography of *Mycobacterium tuberculosis* and implications for tuberculosis product development. *Lancet Infect. Dis.* 7, 328–337. [https://doi.org/10.1016/S1473-3099\(07\)70108-1](https://doi.org/10.1016/S1473-3099(07)70108-1).
- Bottai, D., Frigui, W., Sayes, F., Di Luca, M., Spadoni, D., Pawlik, A., Zoppo, M., Orgeur, M., Khanna, V., Hardy, D., et al. (2020). TbD1 deletion as a driver of the evolutionary success of modern epidemic *Mycobacterium tuberculosis* lineages. *Nat. Commun.* 11, 684. <https://doi.org/10.1038/s41467-020-14508-5>.
- O'Neill, M.B., Shockey, A., Zarley, A., Aylward, W., Eldholm, V., Kitchen, A., and Pepperell, C.S. (2019). Lineage specific histories of *Mycobacterium tuberculosis* dispersal in Africa and Eurasia. *Mol. Ecol.* 28, 3241–3256. <https://doi.org/10.1111/mec.15120>.
- Krishnan, N., Malaga, W., Constant, P., Caws, M., Thi Hoang Chau, T., Salmons, J., Thi Ngoc Lan, N., Bang, N.D., Daffe, M., Young, D.B., et al. (2011). *Mycobacterium tuberculosis* lineage influences innate immune response and virulence and is associated with distinct cell envelope lipid profiles. *PLoS One* 6, e23870. <https://doi.org/10.1371/journal.pone.0023870>.
- Portevin, D., Gagneux, S., Comas, I., and Young, D. (2011). Human macrophage responses to clinical isolates from the *Mycobacterium tuberculosis* complex discriminate between ancient and modern lineages. *PLoS Pathog.* 7, e1001307. <https://doi.org/10.1371/journal.ppat.1001307>.
- Wiens, K.E., and Ernst, J.D. (2016). The Mechanism for Type I Interferon Induction by *Mycobacterium tuberculosis* is Bacterial Strain-Dependent. *PLoS Pathog.* 12, e1005809. <https://doi.org/10.1371/journal.ppat.1005809>.
- Saelens, J.W., Viswanathan, G., and Tobin, D.M. (2019). *Mycobacterial Evolution Intersects With Host Tolerance*. *Front. Immunol.* 10, 528. <https://doi.org/10.3389/fimmu.2019.00528>.
- Ernst, J.D. (2012). The immunological life cycle of tuberculosis. *Nat. Rev. Immunol.* 12, 581–591. <https://doi.org/10.1038/nri3259>.
- Cohen, S.B., Gern, B.H., Delahaye, J.L., Adams, K.N., Plumlee, C.R., Winkler, J.K., Sherman, D.R., Gerner, M.Y., and Urdahl, K.B. (2018). Alveolar Macrophages Provide an Early *Mycobacterium tuberculosis* Niche and Initiate Dissemination. *Cell Host Microbe* 24, 439–446.e4. e434. <https://doi.org/10.1016/j.chom.2018.08.001>.
- Divangahi, M., Behar, S.M., and Remold, H. (2013). Dying to live: how the death modality of the infected macrophage affects immunity to tuberculosis. *Adv. Exp. Med. Biol.* 783, 103–120. https://doi.org/10.1007/978-1-4614-6111-1_6.
- Amaral, E.P., Costa, D.L., Namasivayam, S., Riteau, N., Kamenyeva, O., Mittereder, L., Mayer-Barber, K.D., Andrade, B.B., and Sher, A. (2019). A major role for ferroptosis in *Mycobacterium tuberculosis*-induced cell death and tissue necrosis. *J. Exp. Med.* 216, 556–570. <https://doi.org/10.1084/jem.20181776>.

20. Clay, H., Davis, J.M., Beery, D., Huttenlocher, A., Lyons, S.E., and Ramakrishnan, L. (2007). Dichotomous role of the macrophage in early *Mycobacterium marinum* infection of the zebrafish. *Cell Host Microbe* 2, 29–39. <https://doi.org/10.1016/j.chom.2007.06.004>.
21. Cronan, M., Beerman, R., Rosenberg, A., Saelens, J., Johnson, M., Oehlers, S., Sisk, D., Jurcic Smith, K., Medvitz, N., Miller, S., et al. (2016). Macrophage Epithelial Reprogramming Underlies Mycobacterial Granuloma Formation and Promotes Infection. *Immunity* 45, 861–876. <https://doi.org/10.1016/j.immuni.2016.09.014>.
22. Cronan, M.R., Hughes, E.J., Brewer, W.J., Viswanathan, G., Hunt, E.G., Singh, B., Mehra, S., Oehlers, S.H., Gregory, S.G., Kaushal, D., and Tobin, D.M. (2021). A non-canonical type 2 immune response coordinates tuberculous granuloma formation and epithelialization. *Cell* 184, 1757–1774.e14. <https://doi.org/10.1016/j.cell.2021.02.046>.
23. Davis, J.M., and Ramakrishnan, L. (2009). The role of the granuloma in expansion and dissemination of early tuberculous infection. *Cell* 136, 37–49. <https://doi.org/10.1016/j.cell.2008.11.014>.
24. Lin, P.L., Ford, C.B., Coleman, M.T., Myers, A.J., Gawande, R., Ioerger, T., Sacchettini, J., Fortune, S.M., and Flynn, J.L. (2014). Sterilization of granulomas is common in active and latent tuberculosis despite within-host variability in bacterial killing. *Nat Med* 20, 75–79. <https://doi.org/10.1038/nm.3412>.
25. Behr, M.A., Wilson, M.A., Gill, W.P., Salamon, H., Schoolnik, G.K., Rane, S., and Small, P.M. (1999). Comparative genomics of BCG vaccines by whole-genome DNA microarray. *Science* 284, 1520–1523. <https://doi.org/10.1126/science.284.5419.1520>.
26. Hsu, T., Hingley-Wilson, S.M., Chen, B., Chen, M., Dai, A.Z., Morin, P.M., Marks, C.B., Padiyar, J., Goulding, C., Gingery, M., et al. (2003). The primary mechanism of attenuation of bacillus Calmette-Guerin is a loss of secreted lytic function required for invasion of lung interstitial tissue. *Proc. Natl. Acad. Sci. USA* 100, 12420–12425. <https://doi.org/10.1073/pnas.1635213100>.
27. Mahairas, G.G., Sabo, P.J., Hickey, M.J., Singh, D.C., and Stover, C.K. (1996). Molecular analysis of genetic differences between *Mycobacterium bovis* BCG and virulent *M. bovis*. *J. Bacteriol.* 178, 1274–1282. <https://doi.org/10.1128/jb.178.5.1274-1282.1996>.
28. Pym, A.S., Brodin, P., Brosch, R., Huerre, M., and Cole, S.T. (2002). Loss of RD1 contributed to the attenuation of the live tuberculosis vaccines *Mycobacterium bovis* BCG and *Mycobacterium microti*. *Mol. Microbiol.* 46, 709–717. <https://doi.org/10.1046/j.1365-2958.2002.03237.x>.
29. Lewis, K., Liao, R., Guinn, K., Hickey, M., Smith, S., Behr, M., and Sherman, D. (2003). Deletion of RD1 from *Mycobacterium tuberculosis* mimics bacille Calmette-Guerin attenuation. *J. Infect. Dis.* 187, 117–123. <https://doi.org/10.1086/345862>.
30. Stanley, S.A., Raghavan, S., Hwang, W.W., and Cox, J.S. (2003). Acute infection and macrophage subversion by *Mycobacterium tuberculosis* require a specialized secretion system. *Proc. Natl. Acad. Sci. USA* 100, 13001–13006. <https://doi.org/10.1073/pnas.2235593100>.
31. Augenstein, J., Arbues, A., Simeone, R., Haanappel, E., Wegener, A., Sayes, F., Le Chevalier, F., Chalut, C., Malaga, W., Guilhot, C., et al. (2017). ESX-1 and phthiocerol dimycocerosates of *Mycobacterium tuberculosis* act in concert to cause phagosomal rupture and host cell apoptosis. *Cell Microbiol.* 19, e12726. <https://doi.org/10.1111/cmi.12726>.
32. Conrad, W.H., Osman, M.M., Shanahan, J.K., Chu, F., Takaki, K.K., Cameron, J., Hopkinson-Woolley, D., Brosch, R., and Ramakrishnan, L. (2017). Mycobacterial ESX-1 secretion system mediates host cell lysis through bacterium contact-dependent gross membrane disruptions. *Proc. Natl. Acad. Sci. USA* 114, 1371–1376. <https://doi.org/10.1073/pnas.1620133114>.
33. Manzanillo, P., Shiloh, M., Portnoy, D., and Cox, J. (2012). *Mycobacterium tuberculosis* activates the DNA-dependent cytosolic surveillance pathway within macrophages. *Cell Host Microbe* 11, 469–480. <https://doi.org/10.1016/j.chom.2012.03.007>.
34. Simeone, R., Bobard, A., Lippmann, J., Bitter, W., Majlessi, L., Brosch, R., and Enninga, J. (2012). Phagosomal rupture by *Mycobacterium tuberculosis* results in toxicity and host cell death. *PLoS Pathog.* 8, e1002507. <https://doi.org/10.1371/journal.ppat.1002507>.
35. Groschel, M.L., Sayes, F., Simeone, R., Majlessi, L., and Brosch, R. (2016). ESX secretion systems: mycobacterial evolution to counter host immunity. *Nat. Rev. Microbiol.* 14, 677–691. <https://doi.org/10.1038/nrmicro.2016.131>.
36. Siegrist, M.S., Unnikrishnan, M., McConnell, M.J., Borowsky, M., Cheng, T.Y., Siddiqi, N., Fortune, S.M., Moody, D.B., and Rubin, E.J. (2009). Mycobacterial Esx-3 is required for mycobactin-mediated iron acquisition. *Proc. Natl. Acad. Sci. USA* 106, 18792–18797. <https://doi.org/10.1073/pnas.0900589106>.
37. Serafini, A., Boldrin, F., Palu, G., and Manganelli, R. (2009). Characterization of a *Mycobacterium tuberculosis* ESX-3 conditional mutant: essentiality and rescue by iron and zinc. *J. Bacteriol.* 191, 6340–6344. <https://doi.org/10.1128/JB.00756-09>.
38. Mittal, E., Skowrya, M.L., Uwase, G., Tinaztepe, E., Mehra, A., Koster, S., et al. (2018). *Mycobacterium tuberculosis* Type VII Secretion System Effectors Differentially Impact the ESCRT Endomembrane Damage Response. *mBio* 9, e01765–18. <https://doi.org/10.1128/mBio.01765-18>.
39. Portal-Celhay, C., Tufariello, J.M., Srivastava, S., Zahra, A., Klevorn, T., Grace, P.S., Mehra, A., Park, H.S., Ernst, J.D., Jacobs, W.R., Jr., and Phillips, J.A. (2016). *Mycobacterium tuberculosis* EsxH inhibits ESCRT-dependent CD4(+) T-cell activation. *Nat Microbiol* 2, 16232. <https://doi.org/10.1038/nmicrobiol.2016.232>.
40. Mehra, A., Zahra, A., Thompson, V., Sirisaengtaksin, N., Wells, A., Porto, M., Koster, S., Penberthy, K., Kubota, Y., Dricot, A., et al. (2013). *Mycobacterium tuberculosis* type VII secreted effector EsxH targets host ESCRT to impair trafficking. *PLoS Pathog.* 9, e1003734. <https://doi.org/10.1371/journal.ppat.1003734>.
41. Shah, S., and Briken, V. (2016). Modular Organization of the ESX-5 Secretion System in *Mycobacterium tuberculosis*. *Front. Cell. Infect. Microbiol.* 6, 49. <https://doi.org/10.3389/fcimb.2016.00049>.
42. Gey Van Pittius, N.C., Gamielien, J., Hide, W., Brown, G.D., Siezen, R.J., and Beyers, A.D. (2001). The ESAT-6 gene cluster of *Mycobacterium tuberculosis* and other high G+C Gram-positive bacteria. *Genome biology* 2, RESEARCH0044. <https://doi.org/10.1186/gb-2001-2-10-research0044>.
43. Ates, L.S., Ummels, R., Commandeur, S., van der Weerd, R., Sparrius, M., Weerdenburg, E., Alber, M., Kalscheuer, R., Piersma, S.R., Abdallah, A.M., et al. (2015). Essential Role of the ESX-5 Secretion System in Outer Membrane Permeability of Pathogenic Mycobacteria. *PLoS Genet.* 11, e1005190. <https://doi.org/10.1371/journal.pgen.1005190>.
44. Abdallah, A.M., Verboom, T., Weerdenburg, E.M., Gey van Pittius, N.C., Mahasha, P.W., Jimenez, C., Parra, M., Cadieux, N., Brennan, M.J., Appelmelk, B.J., and Bitter, W. (2009). PPE and PE_PGRS proteins of *Mycobacterium marinum* are transported via the type VII secretion system ESX-5. *Mol. Microbiol.* 73, 329–340. <https://doi.org/10.1111/j.1365-2958.2009.06783.x>.
45. Izquierdo Lafuente, B., Ummels, R., Kuijl, C., Bitter, W., and Speer, A. (2021). *Mycobacterium tuberculosis* Toxin CpnT Is an ESX-5 Substrate and Requires Three Type VII Secretion Systems for Intracellular Secretion. *mBio* 12. <https://doi.org/10.1128/mBio.02983-20>.
46. Person, A.K., Goswami, N.D., Bissette, D.J., Turner, D.S., Baker, A.V., Gadkowski, L.B., Naggie, S., Erlandson, K., Chen, L., Lalani, T., et al. (2010). Pairing QuantiFERON gold in-tube with opt-out HIV testing in a tuberculosis contact investigation in the Southeastern United States. *AIDS patient care and STDs* 24, 539–543. <https://doi.org/10.1089/apc.2010.0102>.
47. Hershberg, R., Lipatov, M., Small, P.M., Sheffer, H., Niemann, S., Homolka, S., Roach, J.C., Kremer, K., Petrov, D.A., Feldman, M.W., and Gagneux, S. (2008). High functional diversity in *Mycobacterium tuberculosis*

- driven by genetic drift and human demography. *PLoS Biol.* 6, e311. <https://doi.org/10.1371/journal.pbio.0060311>.
48. Comas, I., Chakravarti, J., Small, P.M., Galagan, J., Niemann, S., Kremer, K., Ernst, J.D., and Gagneux, S. (2010). Human T cell epitopes of *Mycobacterium tuberculosis* are evolutionarily hyperconserved. *Nat. Genet.* 42, 498–503. <https://doi.org/10.1038/ng.590>.
49. Caws, M., Thwaites, G., Dunstan, S., Hawn, T.R., Thi Ngoc Lan, N., Thuong, N.T.T., Stepniewska, K., Huyen, M.N.T., Bang, N.D., Huu Loc, T., et al. (2008). The influence of host and bacterial genotype on the development of disseminated disease with *Mycobacterium tuberculosis*. *PLoS Pathog.* 4, e1000034. <https://doi.org/10.1371/journal.ppat.1000034>.
50. Click, E.S., Moonan, P.K., Winston, C.A., Cowan, L.S., and Oeltmann, J.E. (2012). Relationship between *Mycobacterium tuberculosis* Phylogenetic Lineage and Clinical Site of Tuberculosis. Clinical infectious diseases: an official publication of the Infectious Diseases Society of America 54, 211–219. <https://doi.org/10.1093/cid/cir788>.
51. Pareek, M., Evans, J., Innes, J., Smith, G., Hingley-Wilson, S., Loughheed, K.E., Sridhar, S., Dedicoat, M., Hawkey, P., and Lalvani, A. (2013). Ethnicity and mycobacterial lineage as determinants of tuberculosis disease phenotype. *Thorax* 68, 221–229. <https://doi.org/10.1136/thoraxjnl-2012-201824>.
52. Seraphin, M.N., Doggett, R., Johnston, L., Zabala, J., Gerace, A.M., and Lauzardo, M. (2017). Association between *Mycobacterium tuberculosis* lineage and site of disease in Florida, 2009–2015. *Journal of molecular epidemiology and evolutionary genetics in infectious diseases* 55, 366–371. <https://doi.org/10.1016/j.meegid.2017.10.004>.
53. Comas, I., Hailu, E., Kiro, T., Bekele, S., Mekonnen, W., Gumi, B., Tschopp, R., Ameni, G., Hewinson, R.G., Robertson, B.D., et al. (2015). Population Genomics of *Mycobacterium tuberculosis* in Ethiopia Contradicts the Virgin Soil Hypothesis for Human Tuberculosis in Sub-Saharan Africa. *Curr. Biol.* : CB 25, 3260–3266. <https://doi.org/10.1016/j.cub.2015.10.061>.
54. Saelens, J.W., Lau-Bonilla, D., Moller, A., Medina, N., Guzman, B., Calderon, M., Herrera, R., Sisk, D.M., Xet-Mull, A.M., Stout, J.E., et al. (2015). Whole genome sequencing identifies circulating Beijing-lineage *Mycobacterium tuberculosis* strains in Guatemala and an associated urban outbreak. *Tuberculosis* 95, 810–816. <https://doi.org/10.1016/j.tube.2015.09.001>.
55. Daleke, M.H., Ummels, R., Bawono, P., Heringa, J., Vandenbroucke-Grauls, C.M.J.E., Luijck, J., and Bitter, W. (2012). General secretion signal for the mycobacterial type VII secretion pathway. *Proc. Natl. Acad. Sci. USA*. 109, 11342–11347. <https://doi.org/10.1073/pnas.1119453109>.
56. Champion, P.A.D., Stanley, S.A., Champion, M.M., Brown, E.J., and Cox, J.S. (2006). C-terminal signal sequence promotes virulence factor secretion in *Mycobacterium tuberculosis*. *Science* 313, 1632–1636. <https://doi.org/10.1126/science.1131167>.
57. Holt, K.E., McAdam, P., Thai, P.V.K., Thuong, N.T.T., Ha, D.T.M., Lan, N.N., Lan, N.H., Nhu, N.T.Q., Hai, H.T., Ha, V.T.N., et al. (2018). Frequent transmission of the *Mycobacterium tuberculosis* Beijing lineage and positive selection for the EsxW Beijing variant in Vietnam. *Nat. Genet.* 50, 849–856. <https://doi.org/10.1038/s41588-018-0117-9>.
58. Walker, T.M., Choisy, M., Dedicoat, M., Drennan, P.G., Wyllie, D., Yang-Turner, F., Crook, D.W., Robinson, E.R., Walker, A.S., Smith, E.G., and Peto, T.E. (2022). *Mycobacterium tuberculosis* transmission in Birmingham, UK, 2009–19: An observational study. *Lancet Reg Health Eur* 17, 100361. <https://doi.org/10.1016/j.lanepe.2022.100361>.
59. Uplekar, S., Heym, B., Friocourt, V., Rougemont, J., and Cole, S.T. (2011). Comparative genomics of Esx genes from clinical isolates of *Mycobacterium tuberculosis* provides evidence for gene conversion and epitope variation. *Infect. Immun.* 79, 4042–4049. <https://doi.org/10.1128/IAI.05344-11>.
60. Elliott, S.R., and Tischler, A.D. (2016). Phosphate starvation: a novel signal that triggers ESX-5 secretion in *Mycobacterium tuberculosis*. *Mol. Microbiol.* 100, 510–526. <https://doi.org/10.1111/mmi.13332>.
61. Shah, S., Cannon, J.R., Fenselau, C., and Briken, V. (2015). A Duplicated ESAT-6 Region of ESX-5 Is Involved in Protein Export and Virulence of *Mycobacteria*. *Infect. Immun.* 83, 4349–4361. <https://doi.org/10.1128/IAI.00827-15>.
62. Stinear, T.P., Seemann, T., Harrison, P.F., Jenkin, G.A., Davies, J.K., Johnson, P.D., Abdallah, Z., Arrowsmith, C., Chillingworth, T., Churcher, C., et al. (2008). Insights from the complete genome sequence of *Mycobacterium marinum* on the evolution of *Mycobacterium tuberculosis*. *Genome Res.* 18, 729–741. <https://doi.org/10.1101/gr.075069.107>.
63. Ates, L.S., van der Woude, A.D., Bestebroer, J., van Stempvoort, G., Musters, R.J.P., Garcia-Vallejo, J.J., Picavet, D.I., Weerd, R.v. d., Mal-etta, M., Kuij, C.P., et al. (2016). The ESX-5 System of Pathogenic *Mycobacteria* Is Involved In Capsule Integrity and Virulence through Its Substrate PPE10. *PLoS Pathog.* 12, e1005696. <https://doi.org/10.1371/journal.ppat.1005696>.
64. Johnson, M.G., and Stout, J.E. (2015). Twenty-eight cases of *Mycobacterium marinum* infection: retrospective case series and literature review. *Infection* 43, 655–662. <https://doi.org/10.1007/s15010-015-0776-8>.
65. Matthews, J.L. (2004). Common diseases of laboratory zebrafish. *Methods Cell Biol.* 77, 617–643. [https://doi.org/10.1016/s0091-679x\(04\)77033-8](https://doi.org/10.1016/s0091-679x(04)77033-8).
66. Sambandamurthy, V.K., Derrick, S.C., Jalapathy, K.V., Chen, B., Russell, R.G., Morris, S.L., and Jacobs, W.R., Jr. (2005). Long-term protection against tuberculosis following vaccination with a severely attenuated double lysine and pantothenate auxotroph of *Mycobacterium tuberculosis*. *Infect. Immun.* 73, 1196–1203. <https://doi.org/10.1128/IAI.73.2.1196-1203.2005>.
67. Rapino, F., Robles, E., Richter-Larrea, J., Kallin, E., Martinez-Climent, J., and Graf, T. (2013). C/EBP α Induces Highly Efficient Macrophage Trans-differentiation of B Lymphoma and Leukemia Cell Lines and Impairs Their Tumorigenicity. *Cell Rep.* 3, 1153–1163. <https://doi.org/10.1016/j.celrep.2013.03.003>.
68. Gaidt, M.M., Morrow, A., Fairgrieve, M.R., Karr, J.P., Yosef, N., and Vance, R.E. (2021). Self-guarding of MORC3 enables virulence factor-triggered immunity. *Nature* 600, 138–142. <https://doi.org/10.1038/s41586-021-04054-5>.
69. Rotty, J.D., Brighton, H.E., Craig, S.L., Asokan, S.B., Cheng, N., Ting, J.P., and Bear, J.E. (2017). Arp2/3 Complex Is Required for Macrophage Integrin Functions but Is Dispensable for FcR Phagocytosis and In Vivo Motility. *Dev. Cell* 42, 498–513.e6. e496. <https://doi.org/10.1016/j.devcel.2017.08.003>.
70. Hetrick, B., Han, M., Helgeson, L., and Nolen, B. (2013). Small molecules CK-666 and CK-869 inhibit actin-related protein 2/3 complex by blocking an activating conformational change. *Chem Biol* 20, 701–712. <https://doi.org/10.1016/j.chembiol.2013.03.019>.
71. Nolen, B.J., Tomasevic, N., Russell, A., Pierce, D.W., Jia, Z., McCormick, C.D., Hartman, J., Sakowicz, R., and Pollard, T.D. (2009). Characterization of two classes of small molecule inhibitors of Arp2/3 complex. *Nature* 460, 1031–1034. <https://doi.org/10.1038/nature08231>.
72. Mackay, E.W., Apschner, A., and Schulte-Merker, S. (2013). A bone to pick with zebrafish. *BoneKey Rep.* 2, 445. <https://doi.org/10.1038/bonekey.2013.179>.
73. Knight, R.D., and Schilling, T.F. (2006). Cranial neural crest and development of the head skeleton. *Adv. Exp. Med. Biol.* 589, 120–133. https://doi.org/10.1007/978-0-387-46954-6_7.
74. Witten, P.E., and Huysseune, A. (2009). A comparative view on mechanisms and functions of skeletal remodelling in teleost fish, with special emphasis on osteoclasts and their function. *Biol. Rev. Camb. Phil. Soc.* 84, 315–346. <https://doi.org/10.1111/j.1469-185X.2009.00077.x>.

75. To, T.T., Witten, P.E., Renn, J., Bhattacharya, D., Huysseune, A., and Winkler, C. (2012). Rankl-induced osteoclastogenesis leads to loss of mineralization in a medaka osteoporosis model. *Development* 139, 141–150. <https://doi.org/10.1242/dev.071035>.
76. Asharani, P.V., Keupp, K., Semler, O., Wang, W., Li, Y., Thiele, H., Yigit, G., Pohl, E., Becker, J., Frommolt, P., et al. (2012). Attenuated BMP1 function compromises osteogenesis, leading to bone fragility in humans and zebrafish. *Am. J. Hum. Genet.* 90, 661–674. <https://doi.org/10.1016/j.ajhg.2012.02.026>.
77. Martinez-Glez, V., Valencia, M., Caparros-Martin, J.A., Aglan, M., Temtamy, S., Tenorio, J., Pulido, V., Lindert, U., Rohrbach, M., Eyre, D., et al. (2012). Identification of a mutation causing deficient BMP1/mTLD proteolytic activity in autosomal recessive osteogenesis imperfecta. *Hum. Mutat.* 33, 343–350. <https://doi.org/10.1002/humu.21647>.
78. Laue, K., Pogoda, H.M., Daniel, P., van Haeringen, A., Alanay, Y., von Arnim, S., Rachwalski, M., Morgan, T., Gray, M., Breuning, M., et al. (2011). Craniosynostosis and multiple skeletal anomalies in humans and zebrafish result from a defect in the localized degradation of retinoic acid. *Am. J. Hum. Genet.* 89, 595–606. <https://doi.org/10.1016/j.ajhg.2011.09.015>.
79. Eames, B.F., Yan, Y.L., Swartz, M.E., Levic, D.S., Knapik, E.W., Postlethwait, J.H., and Kimmel, C.B. (2011). Mutations in *fam20b* and *xylt1* reveal that cartilage matrix controls timing of endochondral ossification by inhibiting chondrocyte maturation. *PLoS Genet.* 7, e1002246. <https://doi.org/10.1371/journal.pgen.1002246>.
80. Simpson, M.A., Hsu, R., Keir, L.S., Hao, J., Sivapalan, G., Ernst, L.M., Zackai, E.H., Al-Gazali, L.I., Hulskamp, G., Kingston, H.M., et al. (2007). Mutations in *FAM20C* are associated with lethal osteosclerotic bone dysplasia (Raine syndrome), highlighting a crucial molecule in bone development. *Am. J. Hum. Genet.* 81, 906–912. <https://doi.org/10.1086/522240>.
81. Johansen, I.S., Nielsen, S.L., Hove, M., Kehrer, M., Shakar, S., Woyen, A.V., Andersen, P.H., Bjerrum, S., Wejse, C., and Andersen, A.B. (2015). Characteristics and Clinical Outcome of Bone and Joint Tuberculosis from 1994 to 2011: A Retrospective Register-Based Study in Denmark, 67 (Clinical infectious diseases : an official publication of the Infectious Diseases Society of America), pp. 554–562. <https://doi.org/10.1093/cid/civ326>.
82. Leonard, M.K., and Blumberg, H.M. (2017). Musculoskeletal Tuberculosis. *Musculoskeletal Tuberculosis. Microbiology spectrum* 5. <https://doi.org/10.1128/microbiolspec.TNMI7-0046-2017>.
83. Barros-Becker, F., Lam, P.Y., Fisher, R., and Huttenlocher, A. (2017). Live imaging reveals distinct modes of neutrophil and macrophage migration within interstitial tissues. *J. Cell Sci.* 130, 3801–3808. <https://doi.org/10.1242/jcs.206128>.
84. Blaser, M.J., and Kirschner, D. (2007). The equilibria that allow bacterial persistence in human hosts. *Nature* 449, 843–849. <https://doi.org/10.1038/nature06198>.
85. Otchere, I.D., Coscolla, M., Sanchez-Buso, L., Asante-Poku, A., Brites, D., Loiseau, C., Meehan, C., Osei-Wusu, S., Forson, A., Laryea, C., et al. (2018). Comparative genomics of *Mycobacterium africanum* Lineage 5 and Lineage 6 from Ghana suggests distinct ecological niches. *Sci. Rep.* 8, 11269. <https://doi.org/10.1038/s41598-018-29620-2>.
86. Fernando, S.L., Saunders, B.M., Sluyter, R., Skarratt, K.K., Goldberg, H., Marks, G.B., Wiley, J.S., and Britton, W.J. (2007). A polymorphism in the *P2X7* gene increases susceptibility to extrapulmonary tuberculosis. *Am. J. Respir. Crit. Care Med.* 175, 360–366. <https://doi.org/10.1164/rccm.200607-970OC>.
87. Xie, X., Li, J., Gu, F., Zhang, K., Su, Z., Wen, Q., Sui, Z., Zhou, P., and Yu, T. (2021). Genetic Determinants for Bacterial Osteomyelitis: A Focused Systematic Review of Published Literature. *Front. Genet.* 12, 654792. <https://doi.org/10.3389/fgene.2021.654792>.
88. Liu, Q., Ma, A., Wei, L., Pang, Y., Wu, B., Luo, T., Zhou, Y., Zheng, H.X., Jiang, Q., Gan, M., et al. (2018). China's tuberculosis epidemic stems from historical expansion of four strains of *Mycobacterium tuberculosis*. *Nat. Ecol. Evol.* 2, 1982–1992. <https://doi.org/10.1038/s41559-018-0680-6>.
89. Stucki, D., Brites, D., Jeljeli, L., Coscolla, M., Liu, Q., Trauner, A., Fenner, L., Rutaiwa, L., Borrell, S., Luo, T., et al. (2016). *Mycobacterium tuberculosis* lineage 4 comprises globally distributed and geographically restricted sublineages. *Nat. Genet.* 48, 1535–1543. <https://doi.org/10.1038/ng.3704>.
90. Blower, S.M., McLean, A.R., Porco, T.C., Small, P.M., Hopewell, P.C., Sanchez, M.A., and Moss, A.R. (1995). The intrinsic transmission dynamics of tuberculosis epidemics. *Nat. Med.* 1, 815–821. <https://doi.org/10.1038/nm0895-815>.
91. Vyazovaya, A., Mokrousov, I., Solovieva, N., Mushkin, A., Manicheva, O., Vishnevsky, B., Zhuravlev, V., and Narvskaya, O. (2015). Tuberculous spondylitis in Russia and prominent role of multidrug-resistant clone *Mycobacterium tuberculosis* Beijing B0/W148. *Antimicrob. Agents Chemother.* 59, 2349–2357. <https://doi.org/10.1128/AAC.04221-14>.
92. Taylor, G.M., Young, D.B., and Mays, S.A. (2005). Genotypic analysis of the earliest known prehistoric case of tuberculosis in Britain. *J. Clin. Microbiol.* 43, 2236–2240. <https://doi.org/10.1128/JCM.43.5.2236-2240.2005>.
93. Krishnan, N., Robertson, B.D., and Thwaites, G. (2010). The mechanisms and consequences of the extra-pulmonary dissemination of *Mycobacterium tuberculosis*. *Mycobacterium tuberculosis. Tuberculosis (Edinb)* 90, 361–366. <https://doi.org/10.1016/j.tube.2010.08.005>.
94. Lieberman, T.D., Wilson, D., Misra, R., Xiong, L.L., Moodley, P., Cohen, T., and Kishony, R. (2016). Genomic diversity in autopsy samples reveals within-host dissemination of HIV-associated *Mycobacterium tuberculosis*. *Nat. Med.* 22, 1470–1474. <https://doi.org/10.1038/nm.4205>.
95. Pepperell, C.S., Casto, A.M., Kitchen, A., Granka, J.M., Cornejo, O.E., Holmes, E.C., Birren, B., Galagan, J., and Feldman, M.W. (2013). The role of selection in shaping diversity of natural *M. tuberculosis* populations. *PLoS Pathog.* 9, e1003543. <https://doi.org/10.1371/journal.ppat.1003543>.
96. Kager, L.M., Runge, J.H., Nederveen, A.J., Roelofs, J.J., Stoker, J., Maas, M., and van der Poll, T. (2014). A new murine model to study musculoskeletal tuberculosis (short communication). *Tuberculosis* 94, 306–310. <https://doi.org/10.1016/j.tube.2014.01.002>.
97. Oehlers, S.H., Cronan, M.R., Scott, N.R., Thomas, M.I., Okuda, K.S., Walton, E.M., Beerman, R.W., Crosier, P.S., and Tobin, D.M. (2015). Interception of host angiogenic signalling limits mycobacterial growth. *Nature* 517, 612–615. <https://doi.org/10.1038/nature13967>.
98. Cambier, C.J., Takaki, K.K., Larson, R.P., Hernandez, R.E., Tobin, D.M., Urdahl, K.B., Cosma, C.L., and Ramakrishnan, L. (2014). *Mycobacteria* manipulate macrophage recruitment through coordinated use of membrane lipids. *Nature* 505, 218–222. <https://doi.org/10.1038/nature12799>.
99. Walton, E.M., Cronan, M.R., Beerman, R.W., and Tobin, D.M. (2015). The Macrophage-Specific Promoter *mfap4* Allows Live, Long-Term Analysis of Macrophage Behavior during *Mycobacterial* Infection in Zebrafish. *PLoS One* 10, e0138949. <https://doi.org/10.1371/journal.pone.0138949>.
100. Singh, S., Holdway, J., and Poss, K. (2012). Regeneration of amputated zebrafish fin rays from de novo osteoblasts. *Dev. Cell* 22, 879–886. <https://doi.org/10.1016/j.devcel.2012.03.006>.
101. Li, H., and Durbin, R. (2010). Fast and accurate long-read alignment with Burrows-Wheeler transform. *Bioinformatics* 26, 589–595. <https://doi.org/10.1093/bioinformatics/btp698>.
102. Larkin, M.A., Blackshields, G., Brown, N.P., Chenna, R., McGettigan, P.A., McWilliam, H., Valentin, F., Wallace, I.M., Wilm, A., Lopez, R., et al. (2007). Clustal W and Clustal X version 2.0. *Bioinformatics* 23, 2947–2948. <https://doi.org/10.1093/bioinformatics/btm404>.
103. Rueden, C.T., Schindelin, J., Hiner, M.C., DeZonia, B.E., Walter, A.E., Arena, E.T., and Eliceiri, K.W. (2017). ImageJ2: ImageJ for the next

- p>generation of scientific image data. BMC Bioinf. 18, 529.
- <https://doi.org/10.1186/s12859-017-1934-z>
- .
104. Schindelin, J., Arganda-Carreras, I., Frise, E., Kaynig, V., Longair, M., Pietzsch, T., Preibisch, S., Rueden, C., Saalfeld, S., Schmid, B., et al. (2012). Fiji: an open-source platform for biological-image analysis. Nat. Methods 9, 676–682. <https://doi.org/10.1038/nmeth.2019>.
 105. Letunic, I., and Bork, P. (2019). Interactive Tree Of Life (iTOL) v4: recent updates and new developments. Nucleic Acids Res. 47, W256–W259. <https://doi.org/10.1093/nar/gkz239>.
 106. Bray, N.L., Pimentel, H., Melsted, P., and Pachter, L. (2016). Near-optimal probabilistic RNA-seq quantification. Nat. Biotechnol. 34, 525–527. <https://doi.org/10.1038/nbt.3519>.
 107. Meijering, E., Dzyubachyk, O., and Smal, I. (2012). Methods for cell and particle tracking. Methods Enzymol. 504, 183–200. <https://doi.org/10.1016/B978-0-12-391857-4.00009-4>.
 108. Stamatakis, A. (2014). RAXML version 8: a tool for phylogenetic analysis and post-analysis of large phylogenies. Bioinformatics 30, 1312–1313. <https://doi.org/10.1093/bioinformatics/btu033>.
 109. Li, H., Handsaker, B., Wysoker, A., Fennell, T., Ruan, J., Homer, N., Marth, G., Abecasis, G., and Durbin, R.; Genome Project Data Processing, S. (2009). The Sequence Alignment/Map format and SAMtools. Bioinformatics 25, 2078–2079. <https://doi.org/10.1093/bioinformatics/btp352>.
 110. Pimentel, H., Bray, N.L., Puente, S., Melsted, P., and Pachter, L. (2017). Differential analysis of RNA-seq incorporating quantification uncertainty. Nat. Methods 14, 687–690. <https://doi.org/10.1038/nmeth.4324>.
 111. Koboldt, D.C., Chen, K., Wylie, T., Larson, D.E., McLellan, M.D., Mardis, E.R., Weinstock, G.M., Wilson, R.K., and Ding, L. (2009). VarScan: variant detection in massively parallel sequencing of individual and pooled samples. Bioinformatics 25, 2283–2285. <https://doi.org/10.1093/bioinformatics/btp373>.
 112. Takaki, K., Davis, J.M., Winglee, K., and Ramakrishnan, L. (2013). Evaluation of the pathogenesis and treatment of Mycobacterium marinum infection in zebrafish. Nat. Protoc. 8, 1114–1124. <https://doi.org/10.1038/nprot.2013.068>.
 113. Cronan, M.R., Rosenberg, A.F., Oehlers, S.H., Saelens, J.W., Sisk, D.M., Jurcic Smith, K.L., Lee, S., and Tobin, D.M. (2015). CLARITY and PACT-based imaging of adult zebrafish and mouse for whole-animal analysis of infections. Dis Model Mech 8, 1643–1650. <https://doi.org/10.1242/dmm.021394>.
 114. Kawakami, K., Takeda, H., Kawakami, N., Kobayashi, M., Matsuda, N., and Mishina, M. (2004). A transposon-mediated gene trap approach identifies developmentally regulated genes in zebrafish. Dev. Cell 7, 133–144. <https://doi.org/10.1016/j.devcel.2004.06.005>.
 115. Balciunas, D., Wangensteen, K.J., Wilber, A., Bell, J., Geurts, A., Sivasubbu, S., Wang, X., Hackett, P.B., Largaespada, D.A., McIvor, R.S., and Ekker, S.C. (2006). Harnessing a high cargo-capacity transposon for genetic applications in vertebrates. PLoS Genet. 2, e169. <https://doi.org/10.1371/journal.pgen.0020169>.
 116. Kwan, K.M., Fujimoto, E., Grabher, C., Mangum, B.D., Hardy, M.E., Campbell, D.S., Parant, J.M., Yost, H.J., Kanki, J.P., and Chien, C.B. (2007). The Tol2kit: a multisite gateway-based construction kit for Tol2 transposon transgenesis constructs. Dev. Dynam. 236, 3088–3099. an official publication of the American Association of Anatomists. <https://doi.org/10.1002/dvdy.21343>.
 117. Yang, X., Boehm, J.S., Yang, X., Salehi-Ashtiani, K., Hao, T., Shen, Y., Lubonja, R., Thomas, S.R., Alkan, O., Bhimdi, T., et al. (2011). A public genome-scale lentiviral expression library of human ORFs. Nat. Methods 8, 659–661. <https://doi.org/10.1038/nmeth.1638>.
 118. Murphy, K.C., Nelson, S.J., Nambi, S., Papavinasundaram, K., Baer, C.E., and Sassetti, C.M. (2018). ORBIT: A New Paradigm for Genetic Engineering of Mycobacterial Chromosomes. mBio 9. <https://doi.org/10.1128/mBio.01467-18>.
 119. Cronin, R.M., Ferrell, M.J., Cahir, C.W., Champion, M.M., and Champion, P.A. (2022). Proteo-genetic analysis reveals clear hierarchy of ESX-1 secretion in Mycobacterium marinum. Proc. Natl. Acad. Sci. USA. 119, e2123100119. <https://doi.org/10.1073/pnas.2123100119>.
 120. Meier, F., Brunner, A.D., Koch, S., Koch, H., Lubeck, M., Krause, M., Goedecke, N., Decker, J., Kosinski, T., Park, M.A., et al. (2018). Online Parallel Accumulation-Serial Fragmentation (PASEF) with a Novel Trapped Ion Mobility Mass Spectrometer. Mol. Cell. Proteomics 17, 2534–2545. <https://doi.org/10.1074/mcp.TIR118.000900>.
 121. Bosserman, R.E., Thompson, C.R., Nicholson, K.R., and Champion, P.A. (2018). Esx Paralogs Are Functionally Equivalent to ESX-1 Proteins but Are Dispensable for Virulence in Mycobacterium marinum. J. Bacteriol. 200, e00726–17. <https://doi.org/10.1128/JB.00726-17>.
 122. Huang, S., Zhou, W., Tang, W., Zhang, Y., Hu, Y., and Chen, S. (2021). Genome-scale analyses of transcriptional start sites in Mycobacterium marinum under normoxic and hypoxic conditions. BMC Genom. 22, 235. 20210406 ed. <https://doi.org/10.1186/s12864-021-07572-8>.
 123. Zulauf, K.E., Sullivan, J.T., and Braunstein, M. (2018). The SecA2 pathway of Mycobacterium tuberculosis exports effectors that work in concert to arrest phagosome and autophagosome maturation. PLoS Pathog. 14, e1007011. <https://doi.org/10.1371/journal.ppat.1007011>.
 124. Thompson, J.D., Gibson, T.J., and Higgins, D.G. (2002). Multiple sequence alignment using ClustalW and ClustalX. Current Protocols in Bioinformatics/Editorial Board. <https://doi.org/10.1002/0471250953.bi0203s00>.
 125. Price, M.N., Dehal, P.S., and Arkin, A.P. (2010). FastTree 2--approximately maximum-likelihood trees for large alignments. PLoS One 5, e9490. <https://doi.org/10.1371/journal.pone.0009490>.
 126. Wertheim, J.O., Murrell, B., Smith, M.D., Kosakovsky Pond, S.L., and Scheffler, K. (2015). RELAX: detecting relaxed selection in a phylogenetic framework. Mol. Biol. Evol. 32, 820–832. <https://doi.org/10.1093/molbev/msu400>.
 127. Letunic, I., and Bork, P. (2021). Interactive Tree Of Life (iTOL) v5: an online tool for phylogenetic tree display and annotation. Nucleic Acids Res. 49, W293–W296. <https://doi.org/10.1093/nar/gkab301>.
 128. Sievers, F., Wilm, A., Dineen, D., Gibson, T.J., Karplus, K., Li, W., Lopez, R., McWilliam, H., Remmert, M., Söding, J., et al. (2011). Fast, scalable generation of high-quality protein multiple sequence alignments using Clustal Omega. Mol. Syst. Biol. 7, 539. <https://doi.org/10.1038/msb.2011.75>.
 129. Waterhouse, A.M., Procter, J.B., Martin, D.M.A., Clamp, M., and Barton, G.J. (2009). Jalview Version 2—a multiple sequence alignment editor and analysis workbench. Bioinformatics 25, 1189–1191. <https://doi.org/10.1093/bioinformatics/btp033>.

STAR★METHODS

KEY RESOURCES TABLE

| REAGENT or RESOURCE | SOURCE | IDENTIFIER |
|--|-------------------------------------|-----------------------------|
| Antibodies | | |
| anti-Arp2 | Abcam | Cat#ab49674; RRID:AB_867730 |
| goat anti-mouse Alexa Fluor 647 | Thermo Fisher | Cat#A21236; RRID:AB_2535805 |
| rabbit anti-HA-Tag | Cell Signaling Technology | Cat#C29F4; RRID:AB_1549585 |
| mouse anti-RNAP | BioLegend | Cat#8RB13; RRID:AB_2566583 |
| Bacterial and virus strains | | |
| <i>Mycobacterium marinum</i> M strain/ pMSP12:cerulean | Oehlers et al. ⁹⁷ | N/A |
| <i>Mycobacterium marinum</i> M strain/ pMSP12:tomato | Cambier et al. ⁹⁸ | N/A |
| <i>Mycobacterium marinum</i> Δ esxM | This paper | N/A |
| <i>Mycobacterium marinum</i> Δ esxM + hsp60:esxM | This paper | N/A |
| <i>Mycobacterium tuberculosis</i> 6020 auxotroph | Sambandamurthy et al. ⁶⁶ | N/A |
| <i>Mycobacterium tuberculosis</i> 6020 + msp12::cerulean | This paper | N/A |
| <i>Mycobacterium tuberculosis</i> 6020 + msp12::cerulean-hsp60:esxM | This paper | N/A |
| <i>Mycobacterium tuberculosis</i> H37Rv | BEI Resources, NIAID | NR-13648 |
| <i>Mycobacterium tuberculosis</i> NCG | This paper | N/A |
| <i>Mycobacterium tuberculosis</i> H37Rv/ msp12:cerulean | This paper | N/A |
| <i>Mycobacterium tuberculosis</i> NCG/ msp12:cerulean | This paper | N/A |
| Chemicals, peptides, and recombinant proteins | | |
| 7H10 | Difco | Cat#262710 |
| Trizol | Ambion | Cat#15596026 |
| Sodium chloride | Fisher Scientific | Cat#S271 |
| Potassium chloride | VWR | Cat#BDH9258 |
| Calcium chloride | VWR | Cat#BDH9224 |
| Magnesium chloride | Ward's Scientific | Cat#470301 |
| 1-phenyl-2-thiourea | Sigma-Aldrich | Cat#P7629 |
| Tricaine-S (MS-222) | Syndel | ANADA#200-226 |
| Low melting point agarose | Fisher Scientific | Cat#BP165-25 |
| CK-666 Arp2/3 inhibitor | Sigma-Aldrich | Cat#182515 |
| CK-689 inactive control | Sigma-Aldrich | Cat#182517 |
| Dimethyl sulfoxide (DMSO) | Fisher Scientific | Cat#BP231 |
| BP Clonase II | Thermo Fisher | Cat#11789020 |
| HyClone HyQTase Cell Detachment Reagent | Fisher Scientific | Cat#SV3003001 |
| DAPI Fluoromount-G | SouthernBiotech | Cat#0100-20 |
| RPMI-1640 | Sigma-Aldrich | Cat#R8758 |
| GlutaMAX Supplement | Thermo Fisher | Cat#35050061 |
| Phorbol-12-myristate-13-acetate (PMA) | Sigma-Aldrich #R8758 | Cat#P148 |
| Sodium pyruvate | Gibco | Cat#11360 |
| Recombinant human IL-3 | Peptotech | Cat#200-03 |

(Continued on next page)

Continued

| REAGENT or RESOURCE | SOURCE | IDENTIFIER |
|--|------------------------------|---------------------------------------|
| Recombinant human M-CSF | Peptrotech | Cat#300-25 |
| β -Estradiol | Sigma-Aldrich | Cat#E2758 |
| Alexa Fluor 555 phalloidin stain | Thermo Fisher | Cat#A34055 |
| Hygromycin B solution | Invitrogen | Cat#10687010 |
| 7H9 | Difco | Cat#271310 |
| OADC | Sigma-Aldrich | Cat#M0678 |
| Neonate-80 | Fisher Scientific | Cat#BP337 |
| TRIzol Reagent | Invitrogen | Cat#15596026 |
| RNase-free DNase I | New England BioLabs | Cat#M0303S |
| Luna universal qPCR master mix | New England BioLabs | Cat#M3003X |
| Tyloxapol | Sigma-Aldrich | Cat#T8761 |
| cOmplete EDTA-free protease inhibitor cocktail | Millipore Sigma | Cat#11836170001 |
| Super-Signal West Pico PLUS | Thermo Fisher | Cat#34580 |
| Super-Signal West Femto Maximum Sensitivity | Thermo Fisher | Cat#34095 |
| Prolong Gold Anti-fade mounting solution | Invitrogen | Cat#P36934 |
| Critical commercial assays | | |
| mMessage mMachine T7 Kit | Thermo Fisher | Cat#AM1344 |
| RNeasy Plus Mini Kit | Qiagen | Cat#74134 |
| Zymo Direct-zol RNA Miniprep Kit | Thomas Scientific | Cat#1159U94 |
| DC Protein Assay Kit | Bio-Rad | Cat#5000111 |
| Pierce Micro BCA Protein Assay Kit | Thermo Fisher | Cat#23235 |
| Deposited data | | |
| <i>Mtb</i> genomic sequencing | NCBI BioProject | PRJNA540867 |
| <i>Mtb</i> H37Rv and NCG RNA sequencing | NCBI BioProject | PRJNA872173 |
| Raw mass spectrometry files | MassIVE repository | MSV000090143 |
| Processed mass spectrometry files | PRIDE repository | PDX036131 |
| Experimental models: Cell lines | | |
| BLaER1 | Rappino et al. ⁶⁷ | N/A |
| RAW 264.7 | ATCC | ATCC product TIB-71 |
| THP-1 | ATCC | ATCC product TIB-202 |
| Experimental models: Organisms/strains | | |
| Zebrafish (<i>Danio rerio</i>), *AB wildtype strain | ZIRC | ZDB-GENO-960809-7 |
| Zebrafish, <i>Tg(mfap4:tomato-caax)</i> ^{xt6} | Walton et al. ⁹⁹ | N/A |
| Zebrafish, <i>Tg(mfap4:esxM-p2a-tdTomato)</i> ^{xt49} | This paper | N/A |
| Zebrafish, <i>Tg(mfap4:esxM_Q59X-p2a-tdTomato)</i> ^{xt50} | This paper | N/A |
| Zebrafish, <i>Tg(mfap4:esxB-p2a-mNeonGreen)</i> ^{xt51} | This paper | N/A |
| Zebrafish, <i>Tg(Ola.Sp7:mCherry-Eco.NfsB)</i> ^{pd46} | Singh et al. ¹⁰⁰ | N/A |
| Zebrafish, <i>Tg(acp5a:mNeonGreen-CAAX)</i> ^{xt52} | This paper | N/A |
| Mouse, C57Bl/6J | Jackson Laboratories | RRID:IMSR_JAX:000,664 |
| Recombinant DNA | | |
| Oligonucleotides | This paper | Available in Table S5 |

(Continued on next page)

Continued

| REAGENT or RESOURCE | SOURCE | IDENTIFIER |
|-------------------------------------|---|---|
| Software and algorithms | | |
| RNA seq analysis original code | This paper | https://doi.org/10.5281/zenodo.6981721 |
| Phylogenetic analysis original code | This paper | https://github.com/vertgenlab/gonomics |
| BWA | Li and Durbin ¹⁰¹ | N/A |
| ClustalW2 | Larkin et al. ¹⁰² | N/A |
| FIJI/ImageJ2, 2.5.0 | Rueden et al. ¹⁰³ ; Schindelin et al. ¹⁰⁴ | N/A |
| iTol | Letunic and Bork ¹⁰⁵ | N/A |
| Kallisto v0.48 | Bray et al. ¹⁰⁶ | N/A |
| MtrackJ, 1.5.1 | Meijering et al. ¹⁰⁷ | N/A |
| RStudio | RStudio Team (2022). RStudio: Integrated Development Environment for R. | N/A |
| RAxML | Stamatakis ¹⁰⁸ | N/A |
| SAMtools | Li et al. ¹⁰⁹ | N/A |
| Sleuth v0.30.0 | Pimentel et al. ¹¹⁰ | N/A |
| VarScan | Koboldt et al. ¹¹¹ | N/A |

RESOURCE AVAILABILITY

Lead contact

Further information and requests for resources should be directed to and will be fulfilled by the lead contact, David Tobin (david.tobin@duke.edu).

Materials availability

All materials and lines generated in this study are available from the lead contact.

Data and code availability

- Genomic sequencing and RNA-seq data are available at NCBI (BioProjects PRJNA540867 and PRJNA872173)
- Raw and processed mass spectrometry files are archived and available at MassIVE and PRIDE repositories under accession numbers MSV000090143 and PDX036131.
- Original code is deposited and publicly available on GitHub and Zenodo. DOIs are listed in the Key Resource Table.
- All other data are available in the main text or supplementary figures.
- Any additional information required to reanalyze the data reported in this work paper is available from the lead contact upon request.

EXPERIMENTAL MODEL AND SUBJECT DETAILS

Ethics statement

All zebrafish husbandry and experiments were approved by the Duke University Animal Care and Use Committee (protocol A091-20-04). Mouse studies were performed in strict accordance using the recommendations from the Guide for the Care and Use of Laboratory Animals of the National Institute of Health and the Office of Laboratory Animal Welfare. Mouse studies were performed at Duke University using protocols approved by the Duke Institutional Animal Care and Use Committee (IACUC) (protocol A221-20-11) in a manner designed to minimize pain and suffering in *M. tuberculosis*-infected animals. Any animal that exhibited severe disease signs was immediately euthanized in accordance with IACUC approved endpoints.

Human subjects

Approval was obtained from the Duke University Medical Center Institutional Review Board to obtain the NCG isolate and to use de-identified clinical data for preparation of the manuscript. The index case was male; the outbreak comprised of three female patients and four male patients, with ages ranging from 25 to 55 years old. Detailed sex and age information is contained in [Figure 1A](#).

Zebrafish husbandry

Zebrafish were maintained on a 14 h light/10 h dark cycle. Water conditions within the system were maintained at 28°C between pH 7.0–7.3 and conductivity 600–700 μ S. Zebrafish were fed twice per day—once per day with dry food and once per day with *Artemia*.

Zebrafish lines

All zebrafish strains used were in the *AB wildtype background. Zebrafish experiments were performed with the approval of the Duke University Animal Care and Use Committee (protocol A091-20-04). Larvae were raised in E3 medium with methylene blue for the first 24 h postfertilization (hpf). Thereafter, larvae were raised in E3 medium supplemented with 45 $\mu\text{g/mL}$ 1-phenyl-2-thiourea (PTU) to halt pigmentation. *Tg(mfap4:tomato-caax)^{xt6}*, *Tg(Ola.Sp7:mCherry-Eco.NfsB)^{pd46}* (a kind gift from Dr. Kenneth Poss's laboratory) have been previously described.^{97,99,100}

Mice

Male C57BL/6J were purchased from the Jackson Laboratory (#0664). All mice were housed in a specific pathogen-free facility under standard conditions (12h light/dark, food and water *ad libitum*). Mice were infected with *Mtb* between 8 and 12 weeks of age. All mice were male.

METHOD DETAILS

Mouse infections

For *in vivo* experiments, 1×10^6 CFU of prepared H37Rv or NCG strains were delivered via i.v. tail vein injection, resulting in an infectious dose (Day 1 CFU) of 10^5 in the spleen and 10^4 in the lung. Groups of 3–4 mice per bacterial strain were infected. At 6 weeks post-infection, mice were euthanized, and organs were harvested then homogenized in a FastPrep-24 (MP Biomedicals). Bacterial burden was quantified by dilution plating half the organ on 7H10 agar and counting colony forming units (CFU) after three weeks of growth. The other half of the lung was placed in trizol, homogenized and frozen until RNA extraction.

Larval and juvenile zebrafish infections

2 dpf larval zebrafish were anesthetized with tricaine (MS-222, final concentration 0.016%). Approximately 200 fluorescent bacteria (FB) of *M. marinum* were injected into the caudal vein of each larval zebrafish with a borosilicate needle. The infected zebrafish were subsequently recovered in E3 medium containing PTU. Any embryos with infection initially seeded above the midline or damaged in the process of injection were removed from the experiment. Fluorescent bacteria were quantified as described in.¹¹² Mixed infection experiments were set up as described above, except that both WT *M. marinum msp12::tdtomato* and ΔesxM *M. marinum msp12::mCerulean* were loaded into the same needle.

Juvenile zebrafish (21 dpf) were anesthetized with tricaine (final concentration 0.016%). Approximately 200 FB were injected into the peritoneum of each juvenile zebrafish using a borosilicate needle. Infected fish were recovered in clean zebrafish system water and maintained in 1 L beakers in an incubator set to 28.5°C with a 14 h light/dark cycle. Animals were fed and observed daily, removing waste and changing over approximately half of the water for fresh fish system water. Fish were monitored for signs of distress and euthanized if they appeared moribund.

PACT clearing of juvenile zebrafish

Juvenile zebrafish were infected as described above. At 2 wpi, zebrafish were euthanized by tricaine overdose and PACT-mediated clearing was performed as previously described.¹¹³

Wound recruitment assays

Larval zebrafish at 3 dpf were anesthetized with tricaine (final concentration 0.016%) and the tail fin was amputated with a sterile no. 11 Miltex razor. For imaging, zebrafish were immobilized in 0.8% low-melt agarose (Fisher BP165) and imaged on an inverted Zeiss axio observer Z1 (20 \times objective, 0.645 $\mu\text{m/pixel}$) immediately for 90 min post-wounding.

Zebrafish drug treatment

Larval zebrafish were infected with *M. marinum* at 2 dpf as described above. At 3dpi, infected zebrafish were treated with 50 μM CK666 (Millipore Sigma) or 50 μM CK689 (Millipore Sigma) for 30 min in media supplemented with 0.5% DMSO. The treated zebrafish were then anesthetized with tricaine (final concentration 0.016%) and mounted in 0.8% low-melt agarose (Fisher BP165) supplemented with the appropriate drug. Zebrafish were imaged for up to 12 h post treatment with an X-Light V2 spinning disk confocal imaging system (Biovision). Migrating macrophages were tracked in ImageJ using the MTrackJ plugin.

Generation of transgenic constructs

To visualize zebrafish osteoclasts, primers (see [methods table](#), *acp5a*-F, *acp5a*-R) containing XhoI (5') and KpnI (3') restriction digest sites were designed to target the 4047 base pair sequence immediately upstream of the tartrate-resistant acid phosphatase gene (*acp5a*) contained on the CH211-276A17 BAC clone obtained from the Children's Hospital Oakland Research Institute (CHORI). The amplicon was cloned into p5E-MCS of the Gateway Cloning system using XhoI and KpnI restriction digest sites. The *acp5a:mNeonGreen*-CAAX transgene was subsequently constructed by recombining p5E *acp5a*, pME mNeonGreen-CAAX and p3E polyA into pDestTol2pA2 to generate pDestTol2; *acp5a:mNeonGreen*-CAAX.

To generate entry clones for expression of mycobacterial proteins (EsxM, truncated EsxM [Q59X]) in zebrafish macrophages, primers targeting the gene sequences were flanked with *attB1* and *attB2* sites and recombined with BP clonase into the pDONR 221 entry clone (see methods table). The EsxB entry clone was derived from the *Mtb* ORFeome (BEI Resources). Macrophage expression constructs were subsequently constructed by recombining: p5E mfap4, pME EsxM, and p3E p2a-tdTomato into pDest-Tol2pA2 to generate pDestTol2; *mfap4:esxM-p2a-tdTomato*; p5E mfap4, pME EsxM (Q59X) and p3E p2a-tdTomato into pDest-Tol2pA2 to generate pDestTol2; *mfap4:esxM(Q59X)-p2a-tdTomato*; and p5E mfap4, pME EsxB, and p3E p2a-mNeonGreen into pDestTol2pA2 to generate pDestTol2; *mfap4:esxB-p2a-mNeonGreen*.

Generation of transgenic zebrafish lines

Transgenic zebrafish were generated via Tol2 transgenesis.¹¹⁴ Tol2 mRNA was generated from T3TS-Tol2¹¹⁵ using an mMessage mMachine kit (Life Technologies). Transgenes were assembled using Gateway Multisite cloning (Invitrogen) according to.¹¹⁶ Single-cell embryos were collected immediately after fertilization and injected with 1 nL of a transgenesis mixture of 25 ng/μL of Tol2 mRNA and 50 ng/μL transgenesis construct. Injected embryos were screened for fluorescence and raised to adulthood. Founders were identified and outcrossed to *AB zebrafish to establish transgenic lines.

RAW 264.7 transwell migration assays

RAW 264.7 macrophages were seeded in 60mm petri dishes to ~80% confluency. Cell concentration was determined, and cells split to seed two 60mm petri dishes with 10⁶ cells/mL and incubated with fresh DMEM +10% FBS at 37°C with 5% CO₂. After 18 h, one plate was infected with the *M. tuberculosis* double deletion auxotrophic strain mc²6020 (*ΔlysAΔpanCD*)⁶⁶ carrying the kanamycin-resistant *msp12::mCerulean* plasmid, and the other was infected with mc²6020 containing the same plasmid with the addition of the *hsp60* promoter driving expression of *esxM*. Each plate was infected at an MOI of 5 and media was supplemented with 24 μg/mL panthothenate and 80 μg/mL L-lysine. Infection occurred over 3 h at 37°C with 5% CO₂. Media was aspirated off, and cells were washed with PBS. Fresh media containing pantothenate, L-lysine and 200 μg/mL gentamicin was added, and cells were incubated at 37°C with 5% CO₂ for 1 h. Cells were starved in DMEM +1% FBS with 20 μg/mL gentamicin, pantothenate, and L-lysine and incubated at 37°C with 5% CO₂ for 18 h. Cells were washed and dislodged with HyQTase (HyClone SV30030-01), and 1 x 10⁶ cells were resuspended in serum-free DMEM with pantothenate and L-lysine into the upper chambers of 24-well transwell plates, with 600 μL of DMEM +10% FBS in the lower chambers. Cells were incubated at 37°C with 5% CO₂. After 20 h of incubation, insert membranes containing migrated cells were fixed with 3.6% PFA and DAPI stained. Fixed membranes were imaged at 2.5× magnification and quantified for cell number using the Zen analysis suite.

RAW 264.7 transduction

The lentiviral vectors for stable macrophage expression of *esxM-3X FLAG* and *cerulean-3X FLAG* were generated through Gateway recombination. The primers targeting the gene sequences were flanked with *attB1* and *attB2* sites and the PCR amplified products were recombined with pDONR 211. Macrophage expression constructs were subsequently generated by recombining pDONR 221: *esxM-3X FLAG*/pDONR 221: *cerulean-3X FLAG* with pLX301. High titer lentivirus packed with the expression vectors were prepared and used to infect RAW 264.7 cells as described.¹¹⁷ RAW 264.7 cells transduced with pLX301: *esxM-3X FLAG*/pLX301: *cerulean-3X FLAG* were selected using 5 μg/mL puromycin.

THP-1 macrophage infection

THP-1 monocytes were cultured at 37°C in 5% CO₂ in RPMI 1640 medium supplemented with 10% (v/v) Fetal bovine serum and 2 mM Glutamax (Gibco). For each experiment, four 10 cm culture dishes treated with 25μg/mL poly-D-Lysine were seeded with the THP-1 cells at a density of 2 x 10⁷ cells per dish, differentiated with 50 ng/mL of phorbol-12-myristate13-acetate (PMA) for two days, and infected 24 h later. The differentiated cells were infected with the single cell suspension of WT *M. marinum::msp12::cerulean* at a MOI of 1:4. After incubation with the bacteria for 4 h at 33°C in 5% CO₂ in antibiotic-free complete RPMI media, cells were washed with 1X PBS and treated with 200 μg/mL gentamicin for 1 h to kill any remaining extracellular bacilli. The cells were then washed in 1X PBS and incubated with complete RPMI containing 20 μg/mL gentamicin at 33°C in 5% CO₂. The cells were harvested at 2 dpi for total RNA isolation.

BLaER1 cell transdifferentiation and infection

BLaER1 cells, a kind gift from T. Graf (Barcelona), were cultured in complete RPMI-1640 medium (supplemented with 2mM L-Glutamine, 1mM Sodium Pyruvate, 100 U/mL Penicillin, 100 μg/mL Streptomycin, and 10% (v/v) heat-inactivated FCS) at 37°C/5%CO₂. They were transdifferentiated in 48-well plates at a concentration of 2.5 x 10⁵ cells/well by using the transdifferentiation media (10 ng/mL hrIL-3 (Peprotech 200-03), 10 ng/mL hr-M-CSF (Peprotech 300-25), 100 nM β-Estradiol (Sigma E2758) in complete RPMI medium) and incubating at 37°C/5%CO₂ for 8 days. The transdifferentiated cells were infected with *Mtb* 6020 *esxM* at MOI 5 and incubated at 37°C/5%CO₂ for 18–20 h. The infected BLaER1 cells were detached from the 48-well plate using HyClone HyQTase (GE Healthcare Life Sciences SV30030.01), spun down, resuspended in complete RPMI and placed on collagen-coated coverslips in 24-well plates. The immunofluorescence assay was performed using Anti-Arp2 antibody (Abcam, ab49674) as primary antibody and goat Anti-mouse Alexa Fluor 647 (Thermo Fisher, A21236) as a secondary antibody plus phalloidin

stain (Alexa Fluor 555, Thermo Fisher A34055). Coverslips were mounted on slides using Mowiol and images were taken with a Zeiss 880 AiryScan or with a Biovision spinning disk confocal microscope. Analysis of the images was performed using FIJI/ImageJ.

Scanning electron microscopy

BLaER1 cells were transdifferentiated in response to 17 β -estradiol in the presence of a cytokine mix (hrIL-3 and hr-M-CSF-1) in 48-well plates for 8 days at 37°C/5%CO₂. Then the cells were infected with either *Mtb* 6020 *msp12::cerulean* or *Mtb* 6020 *msp12::cerulean/hsp60::esxM* at an MOI 5, at 37°C/5%CO₂ for 24h. After that the cells were detached with HyQtase, washed and seeded on 12mm round collagen coated coverslips in a 24-well plate and incubated for 37°C/5%CO₂ for an additional 24h. Cells were fixed with 2.5% glutaraldehyde/0.15M sodium phosphate buffer (pH7.4) at room temperature then processed as described in.⁶⁹

BSL3 infections and analysis using *M. tuberculosis* NCG and H37Rv strains

Wild type BLaER1 cells were cultured in complete RPMI-1640 medium at 37°C/5%CO₂. RPMI 1640 medium supplemented with 2mM L-Glutamine, 1mM Sodium Pyruvate, and 10% (v/v) heat-inactivated FCS. They were transdifferentiated in Poly-D-Lysine (25 μ g/ml) treated Tissue Culture Slides (Mat Tek CCS-4) at a concentration of 2.5 x 10⁵ cells/chamber by using the transdifferentiation media (10 ng/ml hrIL-3 (Peprotech 200-03), 10 ng/ml hr-M-CSF (Peprotech 300-25), 100 nM β -Estradiol (Sigma E2758) in complete RPMI medium) and incubating at 37°C/5%CO₂/7 days. The transdifferentiated cells were infected with *Mtb* NCG *msp12::cerulean* and H37Rv *msp12::cerulean* at MOI 10, incubated at 37°C/5%CO₂/72h and fixed under BSL3 conditions and then stained with Phalloidin (Alexa Fluor Plus 555 A30106). Coverslips were mounted on slides by using Prolong Gold Anti-fade mounting solution (Invitrogen P36934) and images were taken with spinning disk confocal microscopy. Analysis of the images was performed using Fiji.

Bacterial strains

M. marinum strain containing *msp12::tdTomato*⁹⁸ was a kind gift from Lalita Ramakrishnan (University of Cambridge). The *msp12::cerulean* *M. marinum* strain has been previously published.⁹⁷ All strains were grown in either Middlebrook 7H9 media or Middlebrook 7H10 plates supplemented with OADC (10%) and 50 μ g/mL hygromycin and 25 μ g/mL kanamycin. The recombinant *M. tuberculosis* double deletion auxotrophic strains (Δ lysA Δ panCD) *Mtb*₆₀₂₀ *msp12::cerulean* and *Mtb*₆₀₂₀ *hsp60p::esxM/msp12::cerulean* were grown in Middlebrook 7H9 media or Middlebrook 7H10 plates supplemented with OADC (10%), 50 μ g/mL hygromycin, 25 μ g/mL kanamycin, 24 μ g/mL panthothenate and 80 μ g/mL L-lysine as described.⁶⁶ For consistency, single use, frozen aliquots for both the *M. marinum* and *Mtb* strains were prepared for infection as described in.¹¹² All *Mtb* strains used for mouse infections (H37Rv or NCG background) were grown in Middlebrook 7H9 medium containing oleic acid-albumin-dextrose-catalase (OADC), 0.2% glycerol, and 0.05% Tween 80 to log-phase with shaking (200 rpm) at 37°C. Prior to all *in vivo* infections, cultures were washed, resuspended in PBS (PBS) containing 0.05% Tween 80, and sonicated before diluting to desired concentration (see below).

Construction of plasmids

A kanamycin-resistant plasmid containing the *msp12* promoter sequence driving the Cerulean fluorescent protein was constructed for transformation into the hygromycin-resistant Δ esxM *M. marinum* mutant. The hygromycin-resistance gene was excised from the *msp12::cerulean* plasmid that has been previously published (Oehlers et al. 2015) and replaced with the *aph* gene for kanamycin resistance. The kanamycin-resistant *msp12::cerulean* plasmid was amplified using the *msp12::cerulean*_KanR-F and *msp12::cerulean*_KanR-R primers listed in the methods table to complement the Δ esxM *M. marinum* mutant via In-Fusion Cloning (Clontech). Primers were designed to amplify the *hsp60* promoter sequence immediately upstream of *esxM* with a C-terminal HA-tag. Primer sequences used are displayed in Table S5. The two PCR products were joined by In-Fusion cloning.

Generating the *esxM* deletion in *M. marinum*

An *esxM* gene deletion was generated in an *M. marinum* M strain by using the ORBIT system.¹¹⁸ In this system an *esxM* gene targeting oligonucleotide and a payload plasmid were cotransformed into a RecT- and Int-expressing *M. marinum* strain (Mm:pkM444, Addgene #108319) via homologous recombination. A culture of *M. marinum* containing the pKM444 Kan^r plasmid was started overnight by adding 100–150 μ l of fresh saturated stock culture in 30mL 7H9 + 10% OADC +0.05% Tween-80 + 0.2% glycerol +25 μ g/mL Kanamycin in a 125mL flask at 33°C/130rpm/24–48h. At an OD₆₀₀ ~ 0.5, anhydrotetracycline (ATc) was added at a final concentration of 500 ng/mL and incubated again for 8h, then 3mL of 2M Glycine was added to the culture and incubated overnight (19.5h in total after ATc induction). Bacterial cells were spun down in 50mL conical tubes at 4000 rpm/10min/RT and the supernatant was discarded. The pellet was gently resuspended in 2mL of 10% glycerol and then 10% glycerol was added up to 30 mL. Cells were mixed by inverting the tube and spun at 4000 rpm/10min/RT. After the 10% glycerol wash and spin steps were repeated, cells were resuspended in 2 mL 10% glycerol and aliquoted in sterile Eppendorf tubes.

Mm:pkM444 electrocompetent aliquots (380 μ l) were combined with 1 μ g of the attP-containing oligonucleotide targeting *esxM* gene and 200ng of an attB-containing plasmid (pK464 payload plasmid, Addgene #108322). The cells and DNA were mixed by pipetting and transferred to ice-cooled electroporation cuvettes (0.2cm path length). The cells were electroporated with a gene Pulser Xcell set for 25msec (2.5kV, 650 Ω and 50 μ F). After electroporation, the cells were suspended in 900 μ l of 7H9 without antibiotics at

room temperature and up to 2 mL in T25 flasks and incubated overnight at 33°C/130rpm. The next day, two 0.5 mL aliquots of the culture were spread on 7H10 plates with 50 µg/mL Hygromycin and incubated at 33°C/14 days.

The recombinant candidate colonies were picked and streaked on fresh 7H10 plates with 50 µg/mL Hygromycin. The deletion was confirmed by PCR analysis and sequencing. An aliquot of Mm:pKM444 electrocompetent cells with 200 ng of the payload plasmid pKM464 but with no oligomer was used as a negative control. The positive control consisted in Mm:pKM444 electrocompetent cells with 200 ng of the pKM464 plasmid and the rpsL 70mer used to confirm RecT expression and conferring streptomycin resistance.

Protein secretion assays

Protein secretion assays were performed as described previously.¹¹⁹ Briefly, *M. marinum* strains were grown in 7H9 (Middlebrook) broth supplemented with 0.1% Tween 80 and 20 µg/mL Kanamycin to retain the mCerulean plasmid during *in vitro* growth. Cultures were grown to saturation, and sub-cultured to an OD₆₀₀ of 0.8 into 50 mL of Sauton's broth supplemented with Kanamycin and 0.01% Tween 80. After 48 h, the *M. marinum* cells were collected by centrifugation (pellet), and the spent culture media (supernatant) was collected via filtration. The culture supernatant was filtered through 0.2 µm Nalgene Stericup with polyethersulfone (PES) filters and 500 µL of phenylmethylsulfonyl fluoride (PMSF) at a concentration of 174.1 µg/mL. Supernatants were concentrated 50- to 100-fold using a 3 kDa molecular weight cut-off Amicon filter (Millipore). The *M. marinum* cells were resuspended in 500 µL of PBS with PMSF at a concentration of 174.2 µg/mL and lysed using a bead beater (BioSpec). The resulting lysate was clarified by centrifugation. The protein concentrations of the resulting pellet and supernatant fractions were measured using a Micro BCA assay (Pierce).

Proteomics

Short term culture filtrates (described above) of WT:*msp12:cerulean*, Δ *EsxM:msp12:cerulean*, and Δ *EsxM:msp12:cerulean:H-sp60:esxM* were digested with trypsin for proteomics analysis as in.¹¹⁹ Briefly, 100 µg of protein was denatured with 5% SDS, alkylated with iodoacetamide and digested with trypsin using S-Trap reactors (Protifi, NY) according to manufacturer's instructions. Following digestion, peptides were desalted and dried down prior to nano LC-MS/MS analysis as described.

Samples were resuspended in 0.1% formic acid and water, to 1 mg/mL concentration. 100 ng of each sample was injected in triplicate into a Bruker nanoElute and timsTOF Pro LC-MS system. 90-min 600 nL/min gradients were used on a 75 µm × 100 mm PepSep column with C₁₈ ReproSil AQ stationary phase at 1.9 µm particle size, 120 Å pore size. nano-ESI was used as the method of ionization, with a spray voltage of 1700 V. MS was set to Parallel accumulation, serial fragmentation Data Dependent Mode (PASEF-DDA) with a mass range of 100–1700 *m/z*, ion mobility range of 0.6–1.6 v*s/cm², and ramp and accumulation times of 100 ms. Each precursor consisted of 10 PASEF ramps for a cycle time of 1.17 s. Precursors were filtered to contain only charges from 2 to 5. MS/MS collision energy settings were set to ramp from 20 eV at 0.6 ion mobility to 70 eV at 1.6 ion mobility. Instrument tune parameters were set to default for proteomic studies with the following differences: quadrupole low mass set to 20 *m/z*, focus pre-TOF pre-pulse storage set to 5 µs.¹²⁰

Raw '.d' files were subjected to peptide spectral mass matching using MaxQuant and quantification was performed using Label Free Quantification within MaxQuant as in.¹²¹ The most current *M. marinum* FASTA was downloaded from Uniprot and data were filtered to a false discovery rate of 0.01 (1%). Data were normalized to mCerulean and MPT64 to control for cell lysis and sample preparation variances as in.¹²¹ Data were performed in analytical triplicate and biological replicate.

RNA isolation and quantitative RT-PCR analysis

WT *M. marinum* grown in Middlebrook 7H9 media or P₁ low Sauton's media (described elsewhere) was harvested at an OD₆₀₀ of 1 and the pellets were resuspended in RLT plus buffer supplied with the RNeasy Plus kit (QIAGEN). The suspended bacterial pellets were then lysed using 0.7 mm zirconia beads (BioSpec Products) in a BeadBug homogenizer (Benchmark Scientific) at 4000 RPM for 35 s and this process was repeated three more times. Bacterial RNA was then isolated using the RNeasy Plus kit by following the manufacturer's protocol. A similar protocol was followed for the lysis and isolation of total RNA from the WT *M. marinum*-infected THP-1 Monolayers and zebrafish larvae at 2 dpi & 4 dpi respectively. Total RNA was isolated from 50 fish for each experiment. Each fish was infected with a starting dose of ~250 bacilli. *Mtb* H37Rv and NCG grown in Middlebrook 7H9 media were harvested at an OD₆₀₀ of 1 and the pellets were resuspended in TRIzol reagent (Invitrogen). The suspended bacterial pellets were then lysed using 0.7 mm zirconia beads as described previously. Subsequently, bacterial RNA was isolated using the Direct-zol RNA Miniprep kit (Zymo Research) and treated with RNase-free DNase I (NEB). *Mtb* H37Rv and NCG infected mouse lung tissues were harvested at 6 wpi in TRIzol reagent (described elsewhere), and the tissues were initially disrupted in 2 mm zirconia beads followed by the bacterial lysis using 0.7 mm zirconia beads. Total RNA was then isolated using the Direct-zol RNA Miniprep kit as described above.

For *in vitro* grown cultures, 1 µg of RNA was converted into cDNA using the LunaScript RT Super-Mix Kit (NEB). Appropriate no reverse transcriptase controls were included to check for potential DNA contamination. 1 µL of 1:10 diluted cDNA was used as a template for each reaction of quantitative RT-PCR using the Luna Universal qPCR Master Mix (NEB). For *in vivo* infections, total RNA was converted into cDNA as described above and 4 µL of undiluted cDNA was used as a template for each reaction of quantitative RT-PCR. Primers were designed to generate 150 bp – 190 bp amplicons. Due to the very close homology between the *esxM* paralogs of *M. marinum* and *Mtb*, forward primers were designed to anneal to the divergent 5' UTR of their transcripts (Table S5) to differentiate among these paralogs.^{57,122} Transcript levels were normalized to *sigA* for *M. marinum* and *esxM* for *Mtb*.

Protein secretion assay and western blotting

Cultures were initially grown in Middlebrook 7H9 media to log phase and then washed and grown in complete Sauton's media (30 mM DL-asparagine, 7 mM sodium citrate, 3mM potassium phosphate dibasic (Pi), 4 mM magnesium sulfate, 0.2 mM ferric ammonium citrate, 5.7 μ M zinc sulfate, and 4.8% glycerol adjusted to a pH of 7.4) with 0.05% tyloxapol. For experiments performed in P_i -normal condition, bacteria were washed and resuspended in 200 mL of detergent-free complete Sauton's media at an initial OD₆₀₀ of 0.5 and incubated with shaking at 130 RPM for five days at 33°C to an OD₆₀₀ of 0.8–1.0.¹²³ For P_i -low conditions, bacteria were initially cultured in modified Sauton's media containing 250 μ M potassium phosphate dibasic with 0.05% tyloxapol and then washed and grown in 200 mL of detergent-free Sauton's media containing 2.5 μ M potassium phosphate dibasic for 7 days.⁶⁰ Cultures were then centrifuged (3000 x g for 20 min) and culture supernatants and pellets were collected. Culture supernatants were double filtered with Steriflip-GP 0.22 μ m filters (EMD Millipore) and concentrated ~100-fold using Centricon Plus – 70, 3 kDa molecular weight cut-off centrifugal filters (Millipore). Proteins from the culture supernatants were then precipitated using 10% trichloroacetic acid overnight at 4°C and the pellets were washed twice with ice-cold acetone at maximum RPM. The pellets were then resuspended in 250 μ L of extraction buffer (50 mM Tris-Cl – pH 7.5, 6% SDS, and 5 mM EDTA) with cOmplete EDTA-free protease inhibitor cocktail (Sigma-Aldrich). For cell lysate preparation, bacterial pellets were dissolved in 2 mL of extraction buffer with the protease inhibitor cocktail and lysed using 0.7 mm zirconia beads (BioSpec Products). The lysate was then separated from the cellular debris by centrifugation at maximum RPM. The culture filtrate and cell lysate protein concentrations were quantified using the DC protein assay kit (Bio-Rad).

For immunoblot analysis, 30 μ g of culture filtrates and cell lysates were subjected to SDS-PAGE and transferred to the PVDF membrane (Bio-Rad). The membranes were probed with rabbit α -HA-Tag (C29F4, Cell Signaling Technology, 1:1000 dilution) and mouse α -RNAP (8RB13, BioLegend, 1:5000 dilution) overnight at 4°C followed by 1 h incubation at room temperature with appropriate secondary antibodies (goat-*anti*-rabbit (1:5000 dilution), goat-*anti*-mouse (1:2500 dilution) conjugated with HRP, Thermo Scientific). After brief incubation with Super-Signal West Pico PLUS (Thermo Scientific) or Super-Signal West Femto maximum sensitivity Substrate (1:3 dilution, Thermo Scientific), the blots were exposed to Carestream Kodak Biomax MR film (Sigma-Aldrich) for signal detection.

QUANTIFICATION AND STATISTICAL ANALYSIS

RNA sequencing of *M. tuberculosis* bacterial transcripts

Mtb H37Rv and NCG grown in Middlebrook 7H9 media were harvested at an OD₆₀₀ of 1 and the pellets were resuspended in TRIzol reagent (Invitrogen). The suspended bacterial pellets were then lysed using 0.7 mm zirconia beads as described previously. Subsequently, bacterial RNA was isolated using the Direct-zol RNA Miniprep kit (Zymo Research) and treated with RNase-free DNase I (NEB). Library prep using Illumina Stranded Total RNA Prep Ligation with Ribo-Zero Plus (Illumina) was performed by the Duke Center for Genomic and Computational Biology (GCB). The prepared libraries were subsequently sequencing using the NextSeq 500 High-Output platform to generate 75 bp single-end reads.

Transcript abundances were quantified using Kallisto v0.48¹¹³ in single-end mode, with an estimated fragment length of 250 and a SD of 35, and sequence based bias correction. H37Rv cDNA was used as the index for pseudoalignment. Visualization of the data was done in RStudio using Sleuth v0.30.0.¹¹⁰ Raw reads deposited at NCBI in Bioproject PRJNA872173.

Genome assembly and variant calling

The NCG isolate was sequenced on Illumina HiSeq to >500X coverage. Reads are available to download under BioProject ID PRJNA540867. 50 base pair paired-end fastq sequence reads were aligned against the H37Rv reference genome using BWA.¹⁰¹ Variants were called with SAMtools and filtered with VarScan for a minimum read depth of 10, a consensus quality score of 20, and a minimum variant frequency of 0.75.^{111,109} SNPs adjacent to indels were discarded. Drug resistance-associated mutations and genes in repetitive regions (PE/PPE and PGRS) of the genome were discarded, resulting in 31,839 SNPs used for phylogenetic analysis. For lineage analysis, we included SNPs from these regions (35,787 total) since a portion likely represent true variation among global strains.

The reads aligned to *esxM* were inspected manually for every strain included in the initial analysis. Furthermore, the 27 base pair sequence that includes the invariant sequence 10 bp upstream and 14 bp downstream of the TAG stop codon in *esxM* was searched in the fastq files of every isolate included in the initial analysis shown in Figure 2, where the sequence was only found in isolates from the so-called “modern” lineages.

Phylogenetic methods

All trees were based on genome-wide SNPs derived according to the parameters specified above. A superset of SNPs was constructed for each strain with reference alleles occupying sites for which no variants were detected using custom Perl scripts. These SNPs informed neighbor-joining and maximum-likelihood methods of phylogeny construction. Neighbor-joining methodology was implemented with ClustalW2 using pairwise similarity scores of SNP supersets as a measure of genetic distance.¹²⁴ A maximum-likelihood phylogeny was generated with RAxML using a GTR model of nucleotide substitution.¹⁰⁸ For each method, 1000 bootstrap replicates provided support for nodes on the tree. Trees were visualized with FigTree (tree.bio.ed.ac.uk/software/figtree).

When replicating the phylogenetic findings on larger datasets and estimating the selective pressure acting on these genes, we utilized two previously published datasets from Vietnam and Birmingham, UK.^{57,58} We mapped the sequencing reads to the H37Rv reference genome with BWA.¹⁰¹ Similar to the original analysis, we then used SAMtools¹⁰⁹ and VarScan¹¹¹ to call substitutions. We removed libraries where there was support for more than one allele to be called present at the early stop codon in *esxM*, or if there was insufficient support to call either allele as present. We also removed five libraries that did not have both reads available, that could not be confidently assigned to a lineage, or that had an excess of sites that could not be confidently called (SAMN26038068, SAMN26038018, ERR9117709, ERR9117721, SAMN07658239). These filters removed 52 libraries from the UK dataset and none from the Vietnam set. We then used an alignment of only variant sites to construct an approximately maximum likelihood tree.¹²⁵ We then used the RELAX hypothesis testing framework¹²⁶ to calculate the dN/dS rate ratios for both ancestral and modern lineages, as well as assess if there had been a relaxation, or intensification, of the selective pressure in “modern” lineage strains compared to “ancestral” lineage strains. During this hypothesis testing we followed the guidance of the software to remove identical sequences for computational efficiency. We visualized the phylogenies with iTOL.¹²⁷

In silico analyses

Multiple Sequence Alignments were performed using Clustal Omega¹²⁸ and the aligned sequences were visualized using Jalview v2.11.2.0.¹²⁹

Microscopy

Conventional and time-lapse fluorescent microscopy was carried out on a Zeiss Axio Observer Z1 inverted microscope with an Xcite 120Q light source (Lumen Dynamics) and an MRm camera (Zeiss). Imaging of PACT-cleared juvenile zebrafish was performed on an Andor XD spinning disk confocal microscope. Time-lapse and other confocal spinning disk microscopy was performed on a Zeiss Axio Observer Z1 inverted microscope with an X-Light v2 (Crest Optics) imaging system. Images were processed with ImageJ.

Fiji/ImageJ

Infection burden was measured as the number of pixels above background using a constant threshold in ImageJ as described in.¹¹² Dissemination above the midline was defined as colocalization of *M. marinum* and macrophages above the midline at 5 dpi. Following PACT treatment of juvenile zebrafish,¹¹³ animals were scored for dissemination by scanning the spine for fluorescent *M. marinum*. Macrophage migration following partial tail transection was tracked in ImageJ using the MTrackJ plugin. Quantitation of cell culture BLAER1 results was performed using automated plugin “Analyze Particles ...” for Circularity as well as blinded analysis of filopodia frequency.

For Arpc2 cellular distribution analysis, cells were analyzed in ImageJ using in-house Jython scripts. Briefly, macrophage differentiated BLAER1 cells were infected with *M. tuberculosis* mc²6020 expressing either full-length *EsxM* or the mCerulean fluorescent protein. These were imaged singly at 100x, maximum intensity projected, and then a cellular outline is calculated from a channel that is well-distributed across the cell body (in this case, β -actin). This outline is then used to mask the cell and clear any external background. These cells are then visualized in the 3D Surface Plot plugin in FIJI/ImageJ, where the longest X axis is identified and the cells arranged in the XZ orientation along that axis. Smoothing is applied (value = 8.5 in this analysis) and all axes are removed and the background is changed to black before exporting to a static 2D image, which is then used for quantitation by scanning for >0 pixels on a binarized image and writing those coordinates to a.csv, which can then be further analyzed in R. The analysis in R consists of identifying the maximum Y coordinate at each pixel and using that to calculate the area under the curve for each cell across a defined interval of the cell (in percent X distance). Here, our analysis compared the edge 25% of the AUC for each condition, normalized to the AUC for that cell in the middle 50% (25–75%). This allows comparison of the distal/central fluorescence intensity ratio for each cell, which is then plotted in ggplot2. The script allows for arbitrary numbers of cells to be analyzed and compared at once, provided each cell is given a discrete identifier.

Cells were maximum-intensity projected and then the isolated using the “Analyze Particles ...” function. The area outside of the cell was cleared and then the cells were visualized individually using “3D Surface Plot.” These plots were used to identify the longest axis along the cell and then exported to black background RGB images that were then binarized in 8-bit and each data-containing pixel was captured to .csv files. These files were then processed in R to identify the maximum outline of the curves and then the areas under the curve were calculated for each individual cell for a given interval, which were then compared using a t test.

Mass spectrometry statistical analysis

Fold-change data were determined by the ratio of the average of triplicate measurements from the LFQ proteomics data (Table S4). % Coefficient of variation were determined. The propagated average CV for the entire dataset was 8.04% and 8.02% for Δ esxM/WT and Complemented/WT respectively. In cases where protein abundance was significantly determined in one sample (eg WT) but missing in another we limited these values to 2/8 fold-change, the approximate dynamic range of the experiment. Significance was determined using Welch’s modified T test; multiple testing was performed using the Benjamini-Hochberg with an alpha of 0.05. Corrected critical values were $p = 0.0164$, and 0.0200 for Δ esxM/WT and Complemented/WT respectively. Samples were performed in biological duplicate.

Statistics

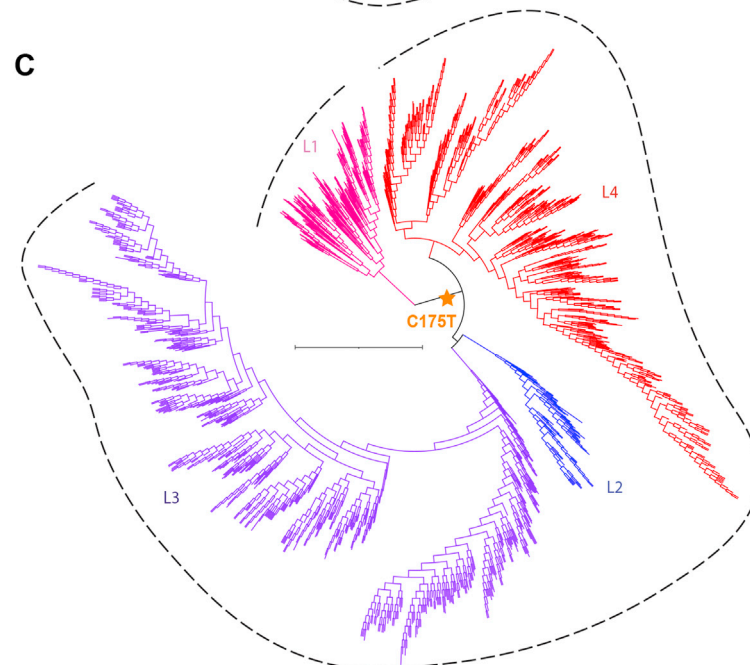
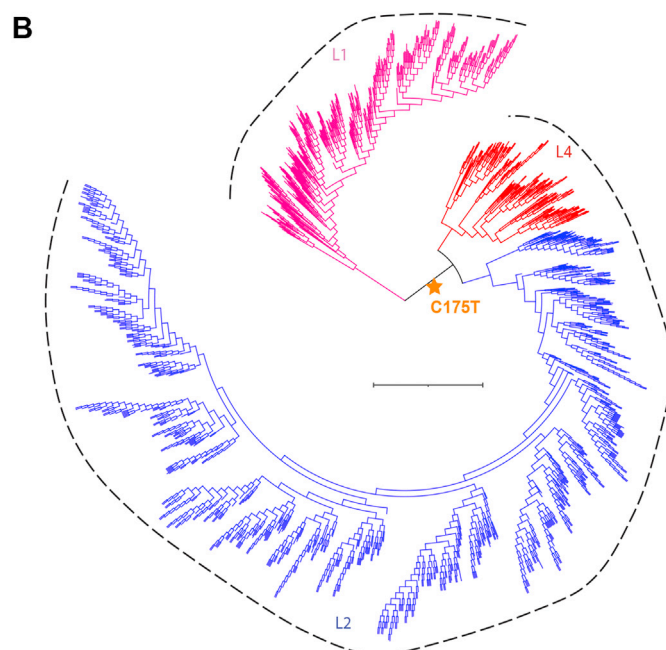
Statistical tests utilized for each experiment are indicated in the figure legends. All statistical analyses were performed using Prism (GraphPad Software) or using R with specified packages when specifically noted.

| Software | |
|---------------------|---|
| Name, Version | Citation |
| BWA | Li and Durbin ¹⁰¹ |
| ClustalW2 | Larkin et al. ¹⁰² |
| Fiji/ImageJ2, 2.5.0 | Schindelin et al. ¹⁰⁴ Rueden et al. ¹⁰³ |
| iTol | Letunic and Bork ¹⁰⁵ |
| Kallisto v0.48 | Bray et al. ¹⁰⁶ |
| MtrackJ, 1.5.1 | Meijering et al. ¹⁰⁷ |
| R studio | RStudio Team (2022). RStudio: Integrated Development Environment for R. |
| RAxML | Stamatakis ¹⁰⁸ |
| SAMtools | Li et al. ¹⁰⁹ |
| Sleuth v0.30.0 | Pimentel et al. ¹¹⁰ |
| VarScan | Koboldt et al. ¹¹¹ |

Supplemental figures

A

| Case number | Spoligotype | MIRU-VNTR |
|-------------|-----------------|--------------|
| 0 | 477777477413771 | 234326223432 |
| 1 | 477777477413771 | 234326223432 |
| 2 | 477777477413771 | 234326223432 |
| 3 | 477777477413771 | 234326223432 |
| 4 | No positive cx | |
| 5 | 477777477413771 | 234326223432 |
| 6 | 477777477413771 | 234326223432 |
| 7 | 477777477413771 | 234326223432 |



(legend on next page)

Figure S1. Outbreak genotyping data and phylogenies of *Mtb* strains from Lineages 1–7, related to Figure 2

(A) Spoligotyping and MIRU-VNTR profile for patient isolates involved in the outbreak.

(B) Approximate maximum likelihood tree of *Mtb* isolates from the Vietnam cohort, visualized with iTOL. Tree scale = 0.01. Gold star indicates the emergence of the shared C175T variant common to all L2, L3, and L4 strains. We also noted two apparent independent reversion events in modern lineages — one in two clustered Lineage 4 and one in two clustered Lineage 2.2 strains - consisting of 4 of the 1,247 “modern” strains in this dataset.

(C) Approximate maximum likelihood tree of *Mtb* isolates from the Birmingham, UK cohort, visualized with iTOL. Tree scale = 0.01. Two independent reversion events in Lineage 4 (5 clustered strains) and Lineage 3 (4 clustered strains) for 9 of 1,392 total in this dataset. Gold star indicates the emergence of the shared C175T variant common to the L2, L3, and L4 strains.

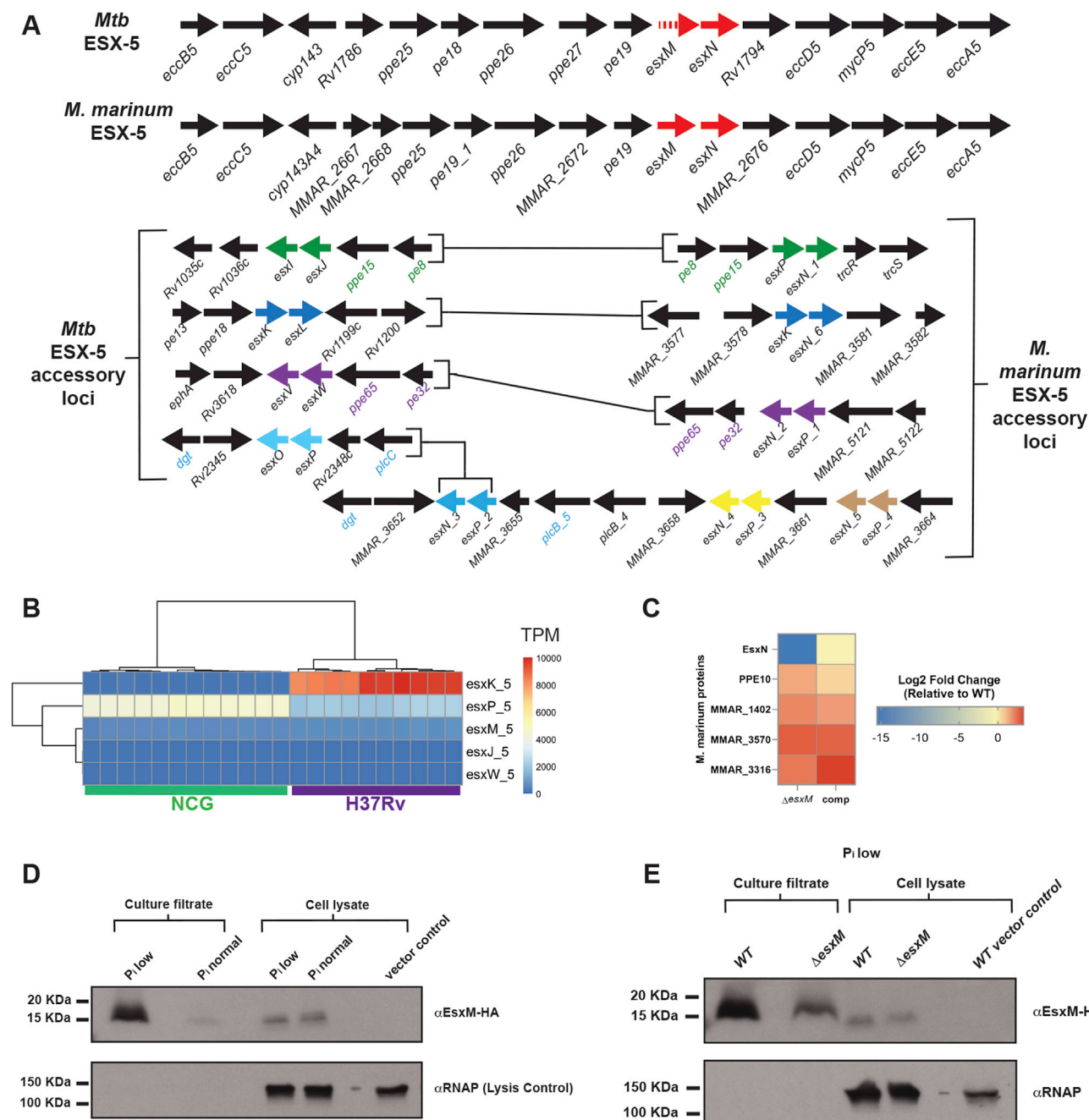


Figure S2. Genome organization, expression and protein secretion analysis for *esxM* and *esxN* paralogs, related to Figure 2

(A) Schematic representing the comparative genome organization of *M. tuberculosis* and *M. marinum* at the main ESX-5 locus and its duplicated *esx* gene loci. The dashed arrow indicates *esxM*'s designation as a pseudogene in H37Rv. Lines mark the paralogous regions of each species based on both sequence conservation and specific examples of synteny of the small Esx proteins in the ESX-5-associated regions. Regions of synteny are indicated by color.

(B) RNA-seq of *Mtb* NCG and H37Rv grown *in vitro*. (C) Mass spectrometry analysis of ESX-5 protein EsxN, and other *M. marinum* secreted proteins.

(D) Western blots of the culture filtrates and cell lysates of WT *M. marinum* expressing HA-tagged *Mtb* EsxM. The strain was cultured in Sauton's medium with either normal phosphate (3 mM KH_2PO_4) or low phosphate (2.5 μM KH_2PO_4) concentrations.

(E) Western blot analysis of the culture filtrates and cell lysates of the WT and Δ *esxM* *M. marinum* expressing EsxM_{Mtb}-HA. Strains were cultured in low phosphate Sauton's medium. Results are representative of two independent experiments. For both D and E, 30 μg of concentrated culture filtrates or cell lysates were loaded and α -RNAP antibody was used as a cell lysis control.

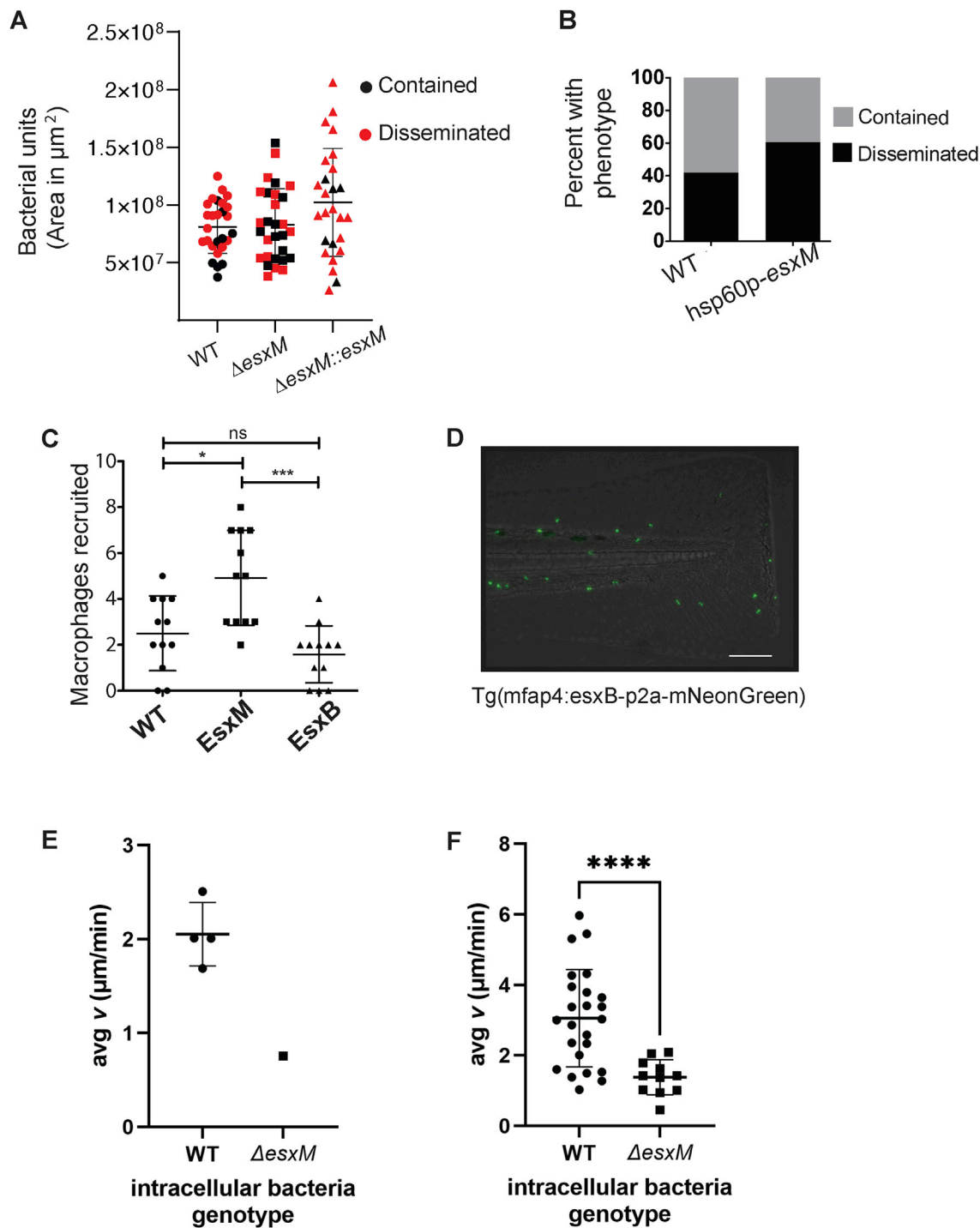


Figure S3. Characterization of infection and secreted effectors in larval zebrafish, related to Figures 3 and 4

(A) Bacterial burden at 5 days post-infection in WT, ΔesxM , and $\Delta\text{esxM}::\text{esxM}$. Black dots indicate samples with infection contained below the midline. Red dots indicate samples with infection above the midline (disseminated). NS by one-way ANOVA with Tukey's multiple comparison test; data are representative of three biological replicates.

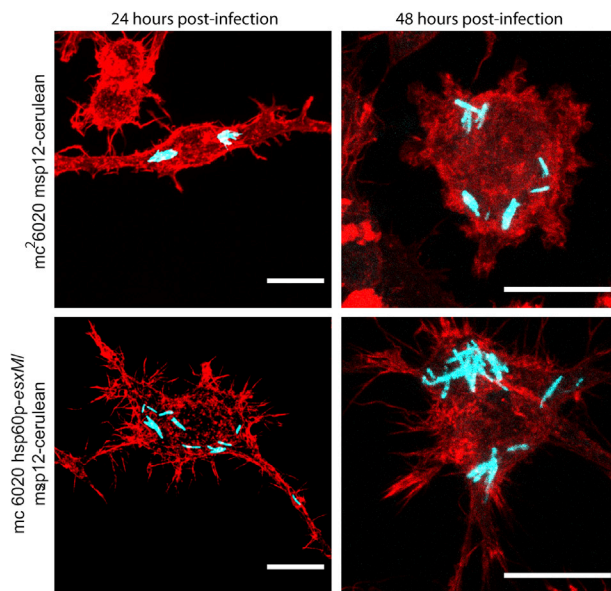
(B) Frequency of dissemination among bacterial infection groups. *M. marinum* over-expressing EsxM in a WT background compared to WT *M. marinum*. $n=31$ WT, 46 hsp60p-esxM

(C) Number of macrophages recruited to tail wound 90 min post-amputation. Macrophages express fluorescent TdTomato, EsxM, or EsxB via a macrophage-specific promoter (mfap4). One-way ANOVA with Dunn's multiple comparison test. Data are representative of three biological replicates.

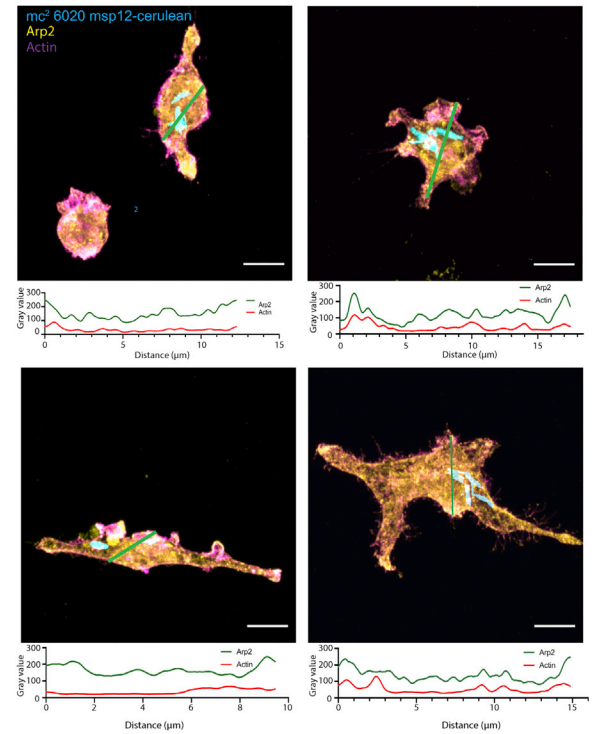
(legend continued on next page)

(D) Representative image of *mfp4:esxB-p2a-mNeonGreen* at 90 min-post amputation. Scale bar, 100 μ m.
(E) Velocity of macrophages infected with WT or Δ *esxM* *M. marinum* egressing from a mixed larval granuloma.
(F) Velocity of macrophages infected with WT or Δ *esxM* *M. marinum* migrating throughout the organism (not confined to a granuloma site). Welch's t test. Data are representative of three biological replicates. Error bars represent mean \pm SD * P < 0.05, **** P < 0.0001.

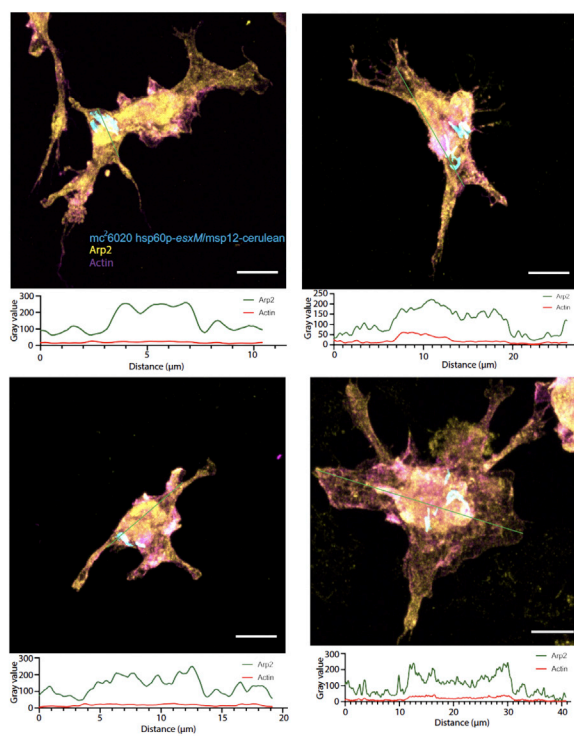
A



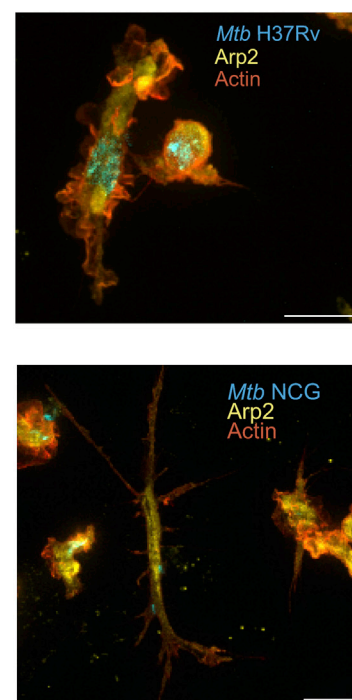
B



C



D



(legend on next page)

Figure S4. RAW 264.7 and BLaER1 cells display unique morphologies when infected with EsxM-expressing *Mtb*₆₀₂₀, and when infected with Lineage 1 or 4 *Mtb* strains, related to Figures 5 and 6

(A) RAW cells infected with *Mtb*₆₀₂₀ *msp12::cerulean* demonstrate fewer cellular projections compared to cells infected with *Mtb*₆₀₂₀ *hsp60p::esxM/msp12::cerulean* at 24- and 48- hours post-infection. Representative of two independent experiments. Scale bar, 15 μ m.

(B) BLaER1 cells infected with *Mtb*₆₀₂₀ *msp12::cerulean* as described in Figure 4 legend. Insets display fluorescence intensity of Arp2 (green) and actin (red) along the green line shown. 8 μ m scale bar.

(C) BLaER1 cells infected with *Mtb*₆₀₂₀ *hsp60p::esxM/msp12::cerulean*. Insets display fluorescence intensity of Arp2 (green) and actin (red) along the green line shown. 8 μ m scale bar.

(D) Additional images of BLaER1 cells infected with *Mtb* H37Rv (top) or *Mtb* NCG (bottom) at 72 h post-infection, representative of two independent experiments. Infection with *Mtb* NCG leads to emergence of spiky membrane projections and a decrease in cellular circularity (as quantified in Figure 6C).

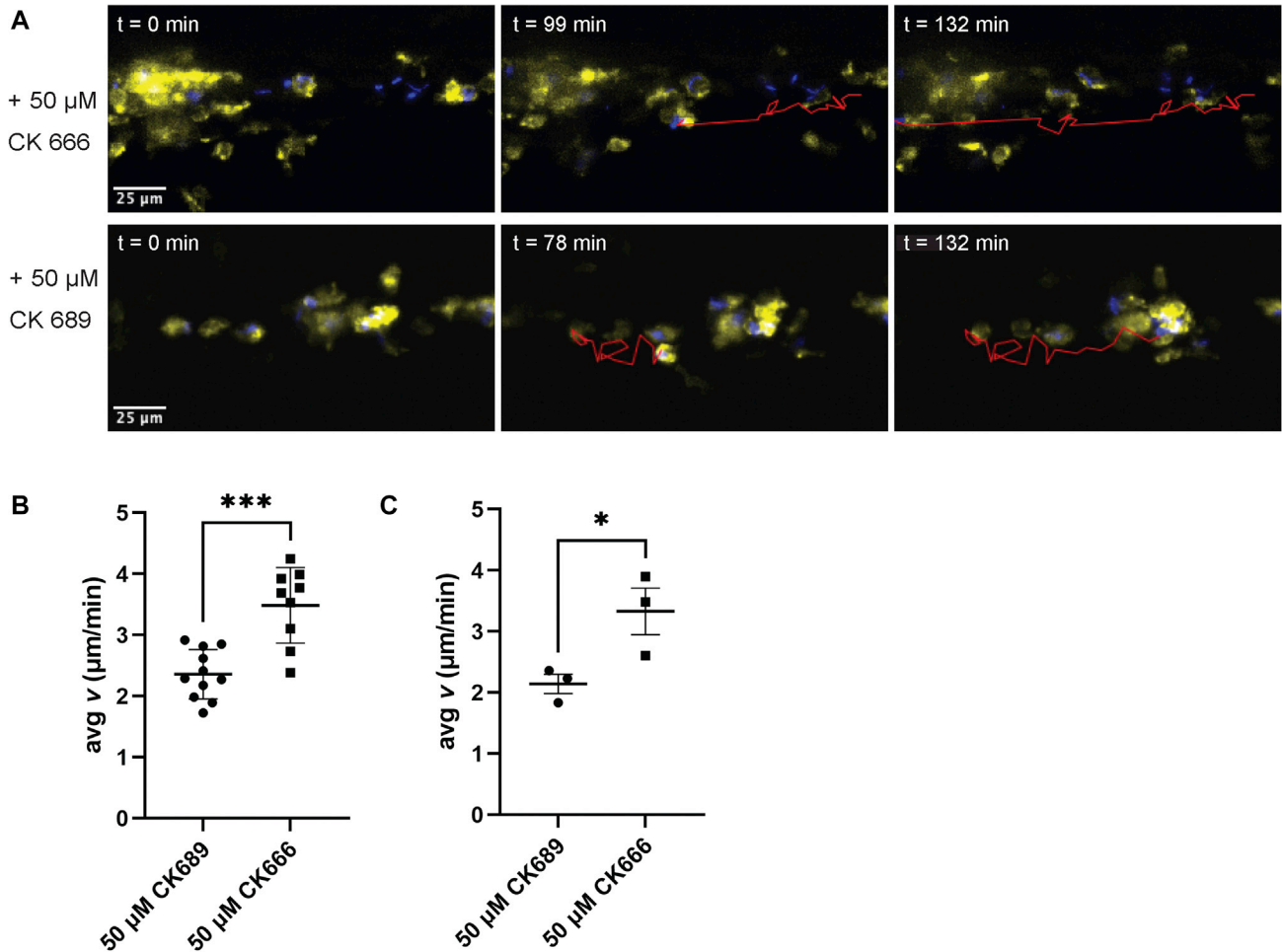


Figure S5. Alterations in Δ esxM infected macrophage velocity upon pharmacological perturbation of Arp2/3, related to Figure 6

(A) Stills from Video S4 showing an infected macrophage in a CK666 treated zebrafish infected with Δ esxM *M. marinum* migrating at an increased rate relative to controls.

(B) Δ esxM *M. marinum*-infected zebrafish larvae treated with control compound CK689 display infected macrophages migrating at a lower velocity relative to CK666 treated macrophages. Quantification of individual macrophages from a single experiment shown; Student's t test, mean \pm SD shown.

(C) Median velocity of all macrophages from three replicate experiments; Student's t test, mean \pm SEM shown. * P < 0.05, *** P = 0.001.